

## Material selection for solar central receiver tubes

M. Laporte-Azcué<sup>\*</sup>, P.A. González-Gómez, M.R. Rodríguez-Sánchez, D. Santana

Energy Systems Engineering Group (ISE), Department of Thermal and Fluid Engineering, University Carlos III of Madrid, Av. Universidad 30, 28911, Spain

### ARTICLE INFO

#### Keywords:

External tubular receiver  
Receiver lifetime  
Levelized cost of alloys  
Tube material selection

### ABSTRACT

The severe operation conditions and great capital investment of solar power tower central receivers motivate the lifetime analysis of a molten-salt external-cylindrical-tubular receiver, considering five alloy alternatives for its tubes manufacturing: Haynes 230, alloy 316H, Inconel 625, 740H and 800H. An analytical low-computational cost methodology is employed, considering the temperature dependence of tube material properties, elastic-plastic stresses/strains and stress relaxation. Thus, creep and fatigue experimental data available in the literature for these alloys are compiled in this work, providing the coefficients required for the methodology followed.

A great alloys operation limitation is the film temperature to avoid corrosion issues; the most permissive are H230, 740H and 800H (650 °C), followed by Inconel 625 (630 °C) and 316H (600 °C). This, and the twice the yield strength, is regarded to set the heliostat field aiming strategy as equatorial as possible for each alloy, resulting in great power production divergences: 24% and 65% less for 625 and alloy 316H receivers with respect to the 740H receiver. Then, the lifetime analysis for a clear design day operation, representative of the receiver during ideal operation, is performed. The stress relaxation regard becomes critical for the accurate damage prediction; alloys 316H and 800H show stress reset during operation, not benefitting from a global stress relaxation. Thus, 800H exhibits a poor endurance. For the clear-day assumption, 740H shows the best lifetime and costs/power performance; the levelized cost of alloy of H230, 625 and alloy 316H is 0.01, 0.09 and over 0.25, respectively, with respect to 740H.

### 1. Introduction

The increasing environmental issues awareness of recent years has encouraged the development and improvement of renewable energy sources for power production, aiming to achieve a significant shift in the traditional energy landscape, which has heavily relied on fossil fuels. Although the goal reaching is still too far, renewable alternatives have experienced a sustained growth in the power generation scenario [1] which is expected to continue in the following years.

Solar power tower (SPTs) technology can integrate cost-effective molten-salt storage and has flexibility on electricity dispatch. SPT plants can play the role of load-following plants like current combined-cycle plants. This is a distinguish feature of SPTs, compared to other variable renewable energies as wind and photovoltaic, where the integration of large batteries is still not competitive with molten-salt thermal storage [2,3]. The SPT feature of providing energy flexibly enables also the participation in ancillary grid services leading to additional revenues and enhancing their competitiveness [4]. SPT plants are constituted by three main subsystems: the heliostat field, the receiver and the power

block. The heliostat field is a series of mirrors (heliostats) provided with sun-tracking devices that concentrate the direct normal irradiance on the receiver surface. The receiver can present different geometries and configurations and work with different heat transfer fluids (HTFs), but it is essentially a heat exchanger that uses the radiation intercepted from the heliostat field to increase the temperature of the HTF through its interior. Then, the power block transforms the energy transferred to the HTF in electricity.

The SPT pilot plant Solar One [5] -which worked with water/steam, had its receiver tubes made of Incoloy 800, and was tested from 1982 to 1984 and then operated until 1987- and the Solar Two pilot plant [6,7] -which operated from 1996 to 1999 with molten salts as HTF and its receiver tubes initially made out of alloy 316- served to gain experience in the design, construction and operation stages of SPT plants, contributing to the further development of this technology and highlighting the issues to tackle in future projects. In Solar One, several tube leaks were detected in the receiver panels [5]. These cracks were due to the weldings that they included, concluding that these needed to be minimized. They were also due to the thermal stresses, caused by the thermal gradients, and the mechanical stresses introduced by the supports that

<sup>\*</sup> Corresponding author.

E-mail address: [mlaporte@ing.uc3m.es](mailto:mlaporte@ing.uc3m.es) (M. Laporte-Azcué).

<https://doi.org/10.1016/j.solmat.2021.111317>

Received 28 January 2021; Received in revised form 30 July 2021; Accepted 31 July 2021

Available online 9 August 2021

0927-0248/© 2021 The Authors.

Published by Elsevier B.V. This is an open access article under the CC BY-NC-ND license

(<http://creativecommons.org/licenses/by-nc-nd/4.0/>).

**Nomenclature**

$a$ :	tube inner wall radius (m)
$A$ :	tube cross section area ( $\text{m}^2$ ), stress relaxation constant ( $\text{Pa}^{-1} \text{s}^{-1}$ )
$b$ :	tube outer wall radius (m)
$c_1, c_2$ :	Manson-Coffin equation exponents
$C$ :	cost (\$)
$C'$ :	creep stress safety factor
$d$ :	damage at the design day
$D$ :	total damage
$E$ :	Young modulus (Pa), thermal energy (MWh)
$H$ :	elasto-plastic modulus (Pa)
$J$ :	total number of creep damage intervals
$k$ :	aiming factor
$K$ :	monotonic strength coefficient (Pa)
$K'$ :	cyclic strength coefficient (Pa)
$L_i$ :	tube length (m)
$m$ :	Norton-Bailey experimental constant
$M$ :	total number of fatigue cycles a day
$n$ :	monotonic strain hardening exponent
$n'$ :	cyclic strain hardening exponent
$n_r$ :	stress power-law for creep strain model
$N$ :	fatigue cycles
$N_p$ :	number of panels
$N_t$ :	number of tubes per panel
$P_i$ :	tube internal pressure (Pa)
$P_T$ :	virtual axial force (N)
$Q$ :	creep activation energy ( $\text{J mol}^{-1}$ )
$r$ :	radial coordinate, radius (m)
$R$ :	ideal gas constant ( $\text{J mol}^{-1} \text{K}^{-1}$ )
$s_p$ :	number of panels substitutions
$S$ :	allowable stress (Pa)
$S_H$ :	hot relaxation strength (Pa)
$S_{SR}$ :	stress reset limit (Pa)
$S_y$ :	yield strength (Pa)
$t$ :	time (hours)
$th$ :	thickness (m)
$T$ :	temperature (K)
$z$ :	axial coordinate

**Greek symbols**

$\alpha$ :	linear thermal expansion coefficient ( $\text{K}^{-1}$ )
$\beta$ :	Mendelson-Roberts-Manson parametrization coefficients
$\Delta P$ :	pressure drop (Pa)
$\Delta t$ :	time interval of creep damage
$\varepsilon$ :	strain (%)
$\varepsilon'_f$ :	fatigue ductility (%)
$\eta_{thermal}$ :	receiver thermal efficiency (%)

$\theta$ :	circumferential coordinate
$\nu$ :	Poisson's ratio
$\sigma$ :	normal stress (Pa)
$\sigma'_f$ :	fatigue strength (%)
$\tau$ :	shear stress (Pa)

**Subscripts**

$a$ :	allowable
$alloy, i$ :	receiver made of alloy i
$c$ :	creep
$cold$ :	cold, room temperature
$creep$ :	effective creep stress
$eq$ :	Von Mises equivalent stress/strain
$f$ :	fatigue
$film$ :	heat transfer fluid region in contact with the tube inner wall
$H$ :	hot relaxation strength
$i$ :	inner tube wall
$L$ :	limit
$M$ :	mechanical stress component
$o$ :	outer tube wall
$P$ :	pressure stress component
$R$ :	rupture
$relax$ :	relaxation
$ref$ :	reference receiver
$stab$ :	stabilization
$T$ :	thermal stress component

**Superindexes**

$E$ :	elastic stress
$P$ :	plastic stress

**Abbreviations**

$AFD$ :	allowable flux density
$ASME$ :	American society of mechanical engineers
$BPVC$ :	boiler and pressure vessel code
$CC$ :	code case
$CSP$ :	concentrating solar power
$DNI$ :	direct normal irradiance ( $\text{W m}^{-2}$ )
$ECGM$ :	energy coarse grid model
$EODs$ :	equivalent operating days
$GPS$ :	generalized plane strain
$HTF$ :	heat transfer fluid
$LCOA$ :	levelized cost of alloy
$LCOE$ :	levelized cost of energy
$LDS$ :	linear damage summation
$M-R-M$ :	Mendelson-Roberts-Manson
$RT$ :	room temperature
$SPT$ :	solar power tower

aimed to prevent the excessive bowing and warpage of the tubes, which also indicated that it was advisable to redesign them in order to allow the tubes to move more freely. In Solar Two, chloride stress corrosion cracking was found on the inside of the receiver tubes, made of alloy 316, suggesting the need to use an advanced material that could successfully resist it [8]. In 1998, one of the original panels was substituted with another one using an advanced high-nickel alloy instead [8]. The location of that specific panel was selected so it endured one of the highest solar flux available on the receiver perimeter. Said panel was then removed from the tower in 2001 after a 15-month use and, with its inspection, its excellent appearance was evident, with no observable leaks or tubes deflection. Moreover, Solar Two showed the successful operation of molten salt receiver and thermal storage [9]. After the

dismantling of these pilot plants, a handful of commercial scale plants using molten salt have operated, such as [10] Gemasolar (Spain, 2011), Crescent Dunes (US, 2015), Atacama-1 (Chile, 2018) or NOOR III (Morocco, 2019), and more instances already being constructed -Redstone Solar Thermal Power Plant in South Africa, DEWA concentrating solar power (CSP) Tower Project in Dubai- or under development -Aurora Solar Energy Project in Australia-. Despite the knowledge acquired after the preceding pilot projects, the great amount of problems happening in the receiver of current operating plants have to do with the salt piping [11], which rank in the third place for the overall facility failure.

Given the elevated cost of the central receiver [12], the demanding conditions that it must endure, such as high heat fluxes and the cyclic

operation, and the inability to use sensors to measure the operation parameters, it has become evident that the development of models as precise as possible is paramount to successfully analyze it and properly predict its correct behaviour under certain operating conditions. Several codes consider the effect of creep, fatigue or creep-fatigue interaction while dealing with providing design guidelines for power boilers [13], such as the R5 British Code [14], the American Society of Mechanical Engineers (ASME) Boiler and Pressure Vessel Code (BPVC) Section III, Subsection NH [15] or the ASME FFS-1 [16]. These present different approaches regarding the consideration of the creep-fatigue interaction, the yield criterion selection or the cyclic hardening/softening, among other aspects. When the SPT technology emerged, the criterion widely accepted to analyze the lifetime of the different plant components, such as the receiver or the steam power generator, was the ASME Code Case (CC) N-47 [17]. For instance, it was used at Solar Two project as reference to obtain the strains and fatigue lifetime [6]. Other example found in the literature of the application of the N-47 CC in the analysis of solar receivers is [18], where the creep and fatigue damages were studied in selected points of a molten salt cavity receiver, with tubes made of Incoloy 800H, resulting that the creep was negligible in comparison with the fatigue damage and the most critical points were found to be the ones under the greatest heat flux and lower HTF temperature. There is another instance in the work of Grossman and Jones [19], where a cavity type molten salt receiver, which was constructed for a 30-year lifetime according to the N-47 and made of Incoloy 800, was studied after a year of testing at SANDIA National Laboratories. From the analysis it was concluded that the damage obtained was excessively high due to the lack of the appropriate material data available in the code and the operating conditions selected. Lastly, Kistler [20] performed a fatigue analysis of a solar central receiver in alloy 316 working with sodium as HTF and using measured weather data as reference. In these last two cases [19,20], the creep damage was considered negligible from the start, being the fatigue mechanism the one regarded as the most relevant in terms of studying the receiver lifetime. Nonetheless, the N-47 CC was conceived for nuclear applications, which meant that it relies on high security margins to assure the reliability of the installation, given the potential damage it can cause in the event an issue occurs. Thus, given the less restrictive conditions in SPT plants, the safety margins of this code were soon found excessive for its use in solar applications, which carried severe economic penalties [21]. Also, the N-47 code case only provided fatigue and creep curves for four types of alloys: 304, 316, Incoloy 800H and 2 1/4 Cr-1 Mo steel [19].

Seeing the need for a specific code for solar components, the N-47 CC was simplified by Berman et al. [21] to make the creep and fatigue damage study more adequate for such technology. Then, Narayanan et al. [22] performed a lifetime analysis of a molten salt receiver made of alloys type 304, type 316 and Incoloy 800, following the modified version [21] of the N-47 code case. The authors considered aspects such as the start-up, the shut down and cloud passages, and the receivers were able to last the expected lifetime of 30 years. Nevertheless, there is no information regarding the stress analysis, performed with a FEA software. A methodology based on the ASME Section III Subsection NH slightly modified is presented by González-Gómez et al. [23], allowing to obtain the stresses under elastic-plastic regime, considering the stress relaxation effect on the material as well. The analysis included, performed for a clear design day of a Haynes 230 molten salt receiver, compares the results obtained with the presented models against FEA simulations, proving the fitness of the proposed methodology. As for sodium receivers, Conroy et al. [24] studied the creep and fatigue damage in a billboard receiver made of different alloys (304, 316 and 800H) following the ASME BPVC: Section III - Subsection NH, slightly modified; the authors found that the first two are more economically appealing despite their worse performance and reliability in comparison with Incoloy 800H. They also demonstrated the importance of the aiming strategy selection in guaranteeing the receiver integrity [25]. Fork et al. [26] analyzed a central receiver made of 617 alloy working

with air as HTF, resulting that creep was the critical damage mechanism over the fatigue one. They used two methods to obtain the damage in the receiver, one based in a modification of the ASME BPVC: Section III - Subsection NH and another one using measured creep-fatigue data. They highlight the influence of the safety factors in the lifetime estimation, which can vary orders of magnitude, and claim that the method selected may result in the underestimation of the fatigue or the creep damages. Lastly, regarding the sCO<sub>2</sub> technology, in which creep becomes a major issue due to the extremely high operating temperatures and pressures, Neises et al. [27] performed an analytical lifetime analysis of the receiver, made of Haynes 230, for different thicknesses and heat fluxes, but they neglected the circumferential variations of the tube wall temperature. Similarly, a sCO<sub>2</sub> receiver in Haynes 230 was also analytically studied by Nithyanandam and Pitchumani [28] for different incident heat fluxes, tube thickness, tube inner radius and mass flow rate. However, the analysis for the creep and fatigue damages was performed separately, in terms of the rupture time due to the creep phenomenon and the number of allowable cycles due to fatigue, and not considering their interaction. Ortega et al. [29] performed a FEA structural analysis of an Inconel 625 sCO<sub>2</sub> receiver tube section, obtaining the accumulated fatigue and creep damage, showing that the former is significantly lower.

In this work, an integral analysis of a molten salt receiver is performed, considering five different alloy alternatives for their manufacturing: Haynes 230, 316H, Inconel 625, Inconel 740H and Incoloy 800H. As mentioned earlier, Incoloy 800H and 316H were used in the Solar One and Solar Two pilot plants respectively, while the remaining alloys exhibit outstanding mechanical and corrosive properties in the operation range of SPT receivers [30–32], motivating their selection. The lifetime of these molten salt receivers is estimated using the analytic method proposed in Ref. [23]. Performing an hourly analysis of a selected clear design day (which is understood as a representative day of the receiver operation during ideal conditions, similarly to the design point approach widely used in the literature [33,34]), the aim is to determine which alloy is the most adequate to be used as the constructive material of the SPT central receiver tubes. This is determined in terms on its predicted lifetime but regarding as well the thermal efficiency and thermal power that can be obtained from its safe operation, which varies among these materials mainly due to their different resistance to the corrosive effects of the molten salts, and seeing how the disparate lifespans obtained for these alloys during such ideal clear day affect the receiver costs. To achieve it, previously developed thermal, mechanical and lifetime models have been used. Aiming for a precise solution, aspects such as the circumferential variation of the tube wall temperature [35], the tube materials properties temperature dependence [36] or the stress relaxation due to creep during hold time [23,37,38] are regarded. Moreover, the creep and fatigue behaviour of the alloys selected is obtained by fitting experimental data available in the literature to the lifetime model equations, providing a compilation of parameters and coefficients that allows the characterization of these materials for future works.

Thus, this manuscript is organized as follows: the heliostat field and thermal model, the elastic stress model and the lifetime one are presented in the various divisions of Section 2, which permit the calculation of the receiver performance and operation from different angles, all of them relevant to properly design it. Moreover, the leveled cost of alloy (LCOA) metric, adequate for the economic analysis, is described. Then, the case of study is presented in Section 3, encompassing the receiver general geometrical and constitutive specifications, as well as the design day chosen and the heliostat field characteristics. The characteristics of the selected alloys, as well as their corresponding creep-fatigue coefficients are also presented in this section. After that, the results for the receiver studied are introduced in Section 4. First, the different aiming strategies are set for the receiver, resulting from performing thermal and elastic stresses analyses. Then, the elastic-plastic stresses and the stress relaxation that lead to the final creep stress are obtained. Closing this

Section, the lifetime prediction for the different receivers and the cost analysis are presented. Lastly, the conclusions constitute Section 5.

## 2. Methodology

The precise receiver lifetime calculation not only relies on the accuracy of the lifetime analysis itself, but also on the upstream calculation of the stresses and strains on the receiver tubes, which in turn depend on the temperature distribution on the tubes and the heat flux reflected by the solar field. The lifetime estimations are key to determine the receiver costs for a certain operation lifespan. In this work, the analysis is performed for a certain clear design day, which is assumed to capture the typical receiver operation conditions at different hour times of the day during the year under ideal conditions (clear-sky day).

Thus, the methodology that leads to the final estimation of the receiver lifetime is presented in this Section, which includes the thermal and structural analysis of the receiver. Then, the LCOA metric, that allows the comparison of the different alloys alternatives in terms of their cost and energy production, is included.

### 2.1. Heliostat field and thermal model

A clear sky model, based on the Daneshyar-Paltridge-Proctor one [39] and that takes into account the solar altitude, allows to obtain the ideal direct normal irradiance (DNI), which is symmetrical with respect to the solar noon. With such DNI, the heat flux on the receiver surface is obtained by using the software tool FluxSPT.<sup>1</sup> Its programming code, developed by Sánchez-González and Santana [40], follows an optical model based on the convolution-projection method. This tool allows to consider various aiming strategies on the receiver surface, permitting to obtain a flat distribution or a more pointed one, which is defined by the aiming factor  $k$ . The aiming factor determines the target point assigned for each heliostat and ranges from 0, which would result in an open aiming (aiming to the top and bottom ends of the receiver), to 3, which is close to be equivalent to an equatorial aiming. In that span, a flat aiming can be found, which would result in the most homogeneous heat flux distribution on the receiver surface as possible [41]. Apart from the heat flux on the receiver, this optical model also provides the optical efficiency of the aiming strategy selected, being greater the higher the  $k$  is (and thus, the more equatorial the aiming is).

Having the heat flux distribution on the receiver surface, the thermal analysis can be undertaken. It has been proven that the circumferential divisions of the tubes cannot be disregarded when aiming a precise solution [42]. It is also relevant to consider the various reflections among the surfaces involved in the radiative exchange in order to obtain an accurate temperature distribution on the tubes [43]. Hence, the tubes studied are discretized in circumferential, radial, and axial divisions for the sake of exactness. The thermal model is based on the ECGM (Energy Coarse Grid Model) presented in Ref. [43], although the thickness is considered fixed so the cases studied can be compared from the most similar initial design point as possible. In the calculations, one tube representative per panel is studied, assuming that all the tubes in a panel are under the same heat flux distribution. The thermal analysis results in the tubes temperature distribution,  $T(\theta, r, z)$ , as well as the thermal power and thermal efficiency of the receiver.

### 2.2. Stress and strain model

Once the temperature distribution on the receiver tubes is obtained, the elastic stresses and strains on them are calculated with the analytic method developed in Ref. [36]. The methodology considers the temperature dependence of the tube material properties. Such dependence has proven to have a significant impact in the stress calculation over the

independent properties consideration and thus it should be taken into account.

At a fixed axial coordinate,  $z$ , the model is based on the separation of the temperature profile in a circumferential distribution,  $\theta$ , and a radial one,  $r$ . The decomposition of the temperature in these two profiles allows us to tackle the problem as the superimposition of the thermal stresses obtained for both cases [44]. Thus, the thermal stresses in the radial and circumferential coordinates are obtained considering the contribution of both effects:  $\sigma_{T,r}^E = \sigma_{T,r}^E + \sigma_{T\theta,r}^E$  and  $\sigma_{T,\theta}^E = \sigma_{T,r}^E + \sigma_{T\theta,\theta}^E$ . Then, the one corresponding to the axial coordinate is obtained by means of the Hooke law as  $\sigma_{T,z}^E = \nu(\sigma_{T,r}^E + \sigma_{T,\theta}^E)$ , considering the plane strain conditions. These loads can be classified as secondary stresses according to ASME [15].

Nevertheless, the thermal gradient on the tube surface not only causes the thermal stresses already presented, but also the deflection of the tubes. To avoid their excessive bending in the radial direction and towards the adjacent tubes, which would lead to hot spots in the potential contact areas, their displacement is restricted with a series of supports, called clips. However, the downside is that these clips introduce mechanical stresses in the axial coordinate,  $\sigma_{M,z}^E$ .

Besides the thermal and mechanical stresses, the pressure of the HTF inside the tubes also contributes to the solicitations that they must endure [45], them being the primary stresses:  $\sigma_{P,r}^E$ ,  $\sigma_{P,\theta}^E$  and  $\sigma_{P,z}^E$ .

Thus, the total stresses on the receiver tubes due to the thermal, mechanical and pressure solicitations are

$$\sigma_r^E = \sigma_{T,r}^E + \sigma_{P,r}^E, \quad (1)$$

$$\sigma_\theta^E = \sigma_{T,\theta}^E + \sigma_{P,\theta}^E,$$

$$\sigma_z^E = \sigma_{T,z}^E + \sigma_{M,z}^E + \sigma_{P,z}^E.$$

In the case of cylindrical external receivers, the dominant stress component,  $\sigma_z$ , is one and two orders of magnitude in comparison to  $\sigma_\theta$  and  $\sigma_r$ , respectively [36]. Given the small entity of the shear stress, a fairly accurate approximation is to consider the normal stresses as equivalent to the principal stresses [36]. Then, the elastic strains,  $\epsilon_\theta$ ,  $\epsilon_r$  and  $\epsilon_z$ , are obtained according to the Hooke law.

Lastly, with the stress and strain components being known and under the generalized plane strain scenario (GPS), the Von Mises equivalent stress and strain are:

$$\sigma_{eq}^E = \sqrt{\frac{(\sigma_r^E - \sigma_\theta^E)^2 + (\sigma_\theta^E - \sigma_z^E)^2 + (\sigma_z^E - \sigma_r^E)^2}{2}} - 3\tau^{E2} \quad (2)$$

$$\epsilon_{eq}^E = \frac{\sqrt{2}}{3} \sqrt{(\epsilon_r^E - \epsilon_\theta^E)^2 + (\epsilon_\theta^E - \epsilon_z^E)^2 + (\epsilon_z^E - \epsilon_r^E)^2} \quad (3)$$

### 2.3. Lifetime model

Thus, the receiver lifetime is estimated by the calculation of the equivalent operating days (EODs), which are the result of considering the creep and fatigue damage mechanisms on the receiver tubes. Creep damage is present during the hold time while fatigue occurs with the cyclic loading. To approach the estimation of the EODs, the widely used linear damage summation (LDS) model is employed [15]. The addition of both the total creep and fatigue damages,  $D_c$  and  $D_f$ , must be equal or lesser than the maximum damage limit allowable:

$$D_L \geq D_c + D_f. \quad (4)$$

Now, if the creep and fatigue damage are obtained for the design day,  $d_c$  and  $d_f$ , the EODs are estimated as

$$D_L = d_c \text{ EODs} + d_f \text{ EODs} \rightarrow \text{EODs} = \frac{D_L}{d_c + d_f}. \quad (5)$$

<sup>1</sup> <http://ise.uc3m.es/research/solar-energy/fluxspt/>.

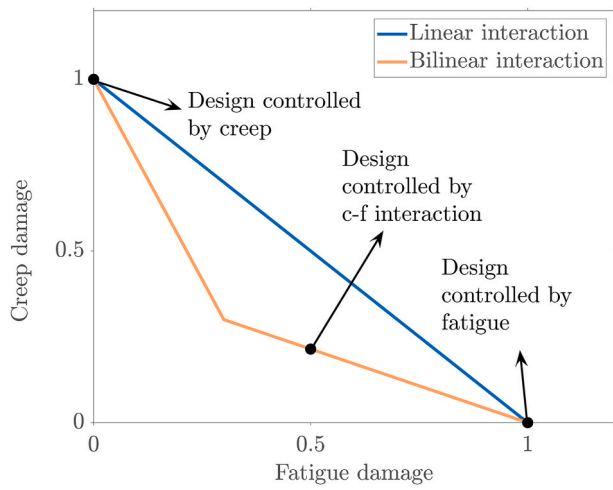


Fig. 1. Creep-fatigue interaction diagram.

On the one hand, the damage limit value varies with the material and it can be equal or lesser than unity. It depends on the bilinear interaction between the creep and fatigue damages and it is typically presented in a creep-fatigue interaction diagram. However, in the LDS method used in this work, the  $D_L$  is considered to have a constant value equal to unity regardless the material used [14,46], becoming the creep-fatigue interaction linear instead of bilinear, Fig. 1. On the other hand, the calculations of the fatigue and creep damages for the design day, which depend on the equivalent elastic stresses and strains, are presented in the following subsections.

### 2.3.1. Creep damage

The creep damage calculation is performed with the rupture time, that depends on the effective creep stress,  $\sigma_{creep}$ . This stress is calculated as

$$\sigma_{creep} = (\sigma_{eq} - \sigma_{relax}) / C' \quad (6)$$

following the ASME Section III, Division 5. Note that, in this work, if  $\sigma_{creep} > \sigma_{eq}$ , the creep stress is taken as  $\sigma_{eq}$  to avoid an excessive level of conservatism. Here  $C'$  is a safety factor set as 0.9, a value suitable for inelastic analysis involving CSP technologies [47,48].  $\sigma_{eq}$  is the elastic-plastic equivalent stress. It is obtained by correcting the elastic stress with the Neuber Method, which allows to consider the plasticity effects of the material, with the yield strength,  $S_y$ , and twice its value delimiting the different regimes:

- For  $\sigma_{eq}^E \leq S_y$ , elastic regime,  $\sigma_{eq} = \sigma_{eq}^E$
- For  $S_y < \sigma_{eq}^E < 2S_y$ , elastic shakedown regime,  $\sigma_{eq}$  is calculated with the Neuber method, in terms of the monotonic stress-strain curve [49], as

$$\sigma_{eq}^E \sigma_{eq} = \frac{\sigma_{eq}^2}{E} + \sigma_{eq} \left( \frac{\sigma_{eq}}{K} \right)^{\frac{1}{n}}, \quad (7)$$

where  $K$  and  $n$  are the monotonic stress-strain curve parameters: the strength coefficient and the strain hardening exponent, respectively, adjusted to experimental data. Their corresponding values for the different alloys studied are presented later in Section 3.2, Table 4.

Alternatively, when the stress-strain curve can be approximated to a bilinear relation, with two linear regions separated by  $S_y$ , it is more accurate to use the Neuber method for an expression that takes into account that linear behaviour of the stress-strain curve [50],

$$\sigma_{eq}^E \sigma_{eq} = \sigma_{eq} \frac{S_y}{E} + \sigma_{eq} \left( \frac{\sigma_{eq} - S_y}{H} \right), \quad (8)$$

being  $H$  the elasto-plastic modulus.

- For  $\sigma_{eq}^E \geq 2S_y$ , reverse plasticity regime, the Neuber method relies on the cyclic stress strain curve, since it takes into account the dynamic material hardening experienced in this regime:

$$\frac{\sigma_{eq}^E \sigma_{eq}}{2} = \frac{\sigma_{eq}^2}{E} + \sigma_{eq} \left( \frac{\sigma_{eq}}{K'} \right)^{\frac{1}{n'}}, \quad (9)$$

in this case, the cyclic strength coefficient,  $K'$ , and the cyclic strain hardening exponent,  $n'$ , are likewise compiled in Table 4.

On the other hand,  $\sigma_{relax}$  is the stress relaxation. It occurs during hold time under a constant peak strain, causing a decrease in the stress of the material [51]. If the hold time of the solicitation at high temperature is high enough, the inelastic nature of creep causes a fraction of the total strain to become permanent. Therefore, the elastic strain decreases, leading to stress relaxation. Neglecting this phenomenon would result in an underestimation of the receiver lifetime [23]. The stress relaxation is obtained by integrating the creep strain rate model (Norton-Bailey) during the dwell period, giving out the expression

$$\sigma_{relax} = \sigma_{eq} - E \left[ \left( \sigma_{eq}/E \right)^{1-n_r} - (1-n_r) A E^{n_r} \exp(-Q/(RT)) \frac{t_{stab}^{m+1}}{m+1} \right]^{1-n_r}. \quad (10)$$

Here  $R$  is the ideal gases constant,  $Q$  is the creep activation energy and  $t_{stab}$  is the stabilization time, in seconds. These and the rest of the parameters are included in Table 5 for the alloys selected. In this work, only the  $T$  and the  $\sigma_{eq}$  of the most critical hour during the day -the combination that result in the greatest stress relaxation- are considered to be causing relaxation on the receiver tubes [23]. This is done for each axial division of the receiver independently, which implies that the critical hour may vary among the axial positions. With such regard, for an hourly study and given the daily cyclic operation of the receiver, the stress relaxation captured in Eq. (10) would only "move forward" 1 h a day, being needed a total of  $t_{stab}$  (expressed in hours in this case) days to achieve such. After the stabilization time, the tubes relaxation is assumed to be totally fulfilled, reaching the global stress relaxation, and such  $\sigma_{relax}$  is then used for all the operation hours during the day to obtain the  $\sigma_{creep}$  according to Eq. (6). However, this stress relaxation during cyclic operation would only be able fully deploy for the whole stabilization time, even with the shutdowns and start-ups of the plant, if there is shakedown to elastic cycling. It occurs if the elastic stress  $\sigma_{eq}^E$  is less than the stress reset limit,  $S_{SR}$ : the addition of the cold yield strength,  $S_{y,cold}$ , and the hot relaxation strength,  $S_H$  [52]. The mentioned  $S_H$  is usually taken as 1.25 $S$ , being  $S$  the allowable stress available at the ASME BPVC Section II Part D [53]. Otherwise, if  $\sigma_{eq}^E > S_{y,cold} + S_H$ , stress reset occurs after the daily shutdown, which means that the initial stress level is restored the following day. This would be equal to having a total  $t_{stab}$  of just 1 h, given that the stress relaxation would not be daily accumulated.

Once the  $\sigma_{creep}$  is known, there are several formulations to obtain the rupture time [54]. In this work, it is calculated with the Mendelson-Roberts-Manson (M-R-M) parametrization,

$$\log_{10}(t_R) = \beta_0 + \beta_1 \frac{1}{T} + \beta_2 \log_{10}(\sigma_{creep}) + \beta_3 \log_{10}(\sigma_{creep})^{\frac{1}{T}}. \quad (11)$$

The M-R-M coefficients,  $\beta$ , are presented in Table 6. It should be noted that in Eq. (11)  $\sigma_{creep}$  is introduced in MPa while the temperature is in K, resulting in a rupture time expressed in hours. Unlike the Larson-Miller parametrization, the M-R-M one does not have any coefficient fixed to zero, which gives it a good degree of flexibility. It also considers the temperature dependence as reciprocal, which is suitable given that, in most creep mechanisms, the diffusion involved is an Arrhenius-type one [54].

Lastly, the creep damage for the design day is obtained by adding the ratios of time intervals,  $\Delta t_j$ , over their corresponding time to rupture,

$t_{R,j}$ :

$$d_c = \sum_{j=1}^J \frac{\Delta t_j}{t_{R,j}} \quad (12)$$

A time interval is a period at which the receiver tubes are subjected to a constant creep stress and temperature, resulting in a specific time to rupture.  $J$  is the total number of time intervals occurring in the design day.

### 2.3.2. Fatigue damage

The fatigue damage is estimated after the number of allowable cycles, which varies with the strain range. Thus, the equivalent elastic-plastic strain range is calculated as follows, similarly to the equivalent elastic-plastic stress:

- For  $\sigma_{eq}^E < 2S_y$ ,  $\Delta \varepsilon_{eq} = \Delta \varepsilon_{eq}^E$ ,
- For  $\sigma_{eq}^E \geq 2S_y$ , the equivalent elastic-plastic stress range ( $\Delta \sigma_{eq}$ ) is obtained following the Neuber method

$$\Delta \sigma_{eq}^E \Delta \varepsilon_{eq}^E = \frac{\Delta \sigma_{eq}^2}{E} + 2 \Delta \sigma_{eq} \left( \frac{\Delta \sigma_{eq}}{2K'} \right)^{\frac{1}{n}} \quad (13)$$

After that, the equivalent plastic strain range ( $\Delta \varepsilon_{eq}^P$ ) is calculated as [55]

$$\Delta \varepsilon_{eq}^P = 2 \left( \frac{\Delta \sigma_{eq}}{2K'} \right)^{\frac{1}{n}}, \quad (14)$$

and then the equivalent elastic-plastic strain range ( $\Delta \varepsilon_{eq}$ ) is obtained as [56]

$$\Delta \varepsilon_{eq} = \frac{\Delta \sigma_{eq}}{E} + \Delta \varepsilon_{eq}^P \quad (15)$$

With  $\Delta \varepsilon_{eq}$ , the number of allowable cycles,  $N_a$ , is calculated using the implicit Manson-Coffin expression,

$$\frac{\Delta \varepsilon_{eq}}{2} = \frac{\Delta \varepsilon_{eq}^E}{2} + \frac{\Delta \varepsilon_{eq}^P}{2} = \frac{\sigma'_f}{E} N_a^{-c_1} + \varepsilon'_f N_a^{-c_2}, \quad (16)$$

where  $\varepsilon'_f$  is the fatigue ductility of the material and  $\sigma'_f$  is the fatigue strength coefficient. Their values, as well as the ones of the exponents  $c_1$  and  $c_2$ , are included in Table 7 for the alloys studied. A number of cycles low enough to make  $\Delta \varepsilon_{eq}^P \gg \Delta \varepsilon_{eq}^E$  implies a plastic cyclic straining where

$\Delta \varepsilon_{eq}$  is equivalent to consider only its plastic component,  $\frac{\Delta \varepsilon_{eq}}{2} \approx \frac{\Delta \varepsilon_{eq}^P}{2} = \varepsilon'_f N_a^{-c_2}$ . On the contrary, a high number of cycles that satisfies  $\Delta \varepsilon_{eq}^E \gg \Delta \varepsilon_{eq}^P$  results in an elastic cyclic straining, with  $\frac{\Delta \varepsilon_{eq}}{2} \approx \frac{\Delta \varepsilon_{eq}^E}{2} = \frac{\sigma'_f}{E} N_a^{-c_1}$ . As it can be perceived from the resulting equations, in the first case fatigue is ductility controlled while in the second case it is strength controlled.

Having the number of allowable cycles, the fatigue damage of the design day is defined as the summation of the ratios between the number of fatigue cycles,  $N$ , and their corresponding number of allowable cycles,  $N_a$ , resulting at their respective equivalent strain range conditions:

$$d_f = \sum_{m=1}^M \frac{N_m}{N_{a,m}} \quad (17)$$

### 2.4. Levelized cost of alloy (LCOA)

The metric selected to analyze the cost of each alloy as the centric element of the SPT receiver is the levelized cost of alloy (LCOA), obtained as

$$LCOA_i = \frac{C_{alloy,i} - C_{alloy,ref}}{E_{alloy,i}} + C_{ref} \left( \frac{1}{E_{alloy,i}} - \frac{1}{E_{ref}} \right) \quad (18)$$

This is a similar approach to the one introduced in Ref. [57] for the

coating analysis. Since, unlike the coating, the receiver would not be able to work without the tubes, one of the studied receivers (or alloys) needs to be fixed as the reference one. Consequently, the LCOA for such receiver would be zero and the LCOA of the receiver in alloy  $i$  is the result of the difference between its levelized cost of energy (LCOE) and the LCOE of the reference receiver (with its tubes and headers made of the reference alloy), only considering the costs derived from the tubes installation and substitutions.

Here,  $C_{alloy,i}$  is the annualized cost of alloy  $i$  and  $E_{alloy,i}$  is the annualized energy production of such receiver, considering 300 EODs per year and 11 h of daily operation. On the other hand,  $C_{ref}$  and  $E_{ref}$  are the annualized total cost of the reference receiver and its annualized energy production, respectively, while  $C_{alloy,ref}$  is just the annualized cost of the alloy involved in the reference receiver.

## 3. Case of study

In this Section, the receiver design characteristics are presented. The configurations differ only in the constitutive material of the tubes. The mechanical coefficients required for the receiver lifetime calculation, which vary for the alloys studied, are presented in Section 3.2. Such material alternatives will be later analyzed under a certain design day, which is introduced in Section 3.3, in order to perform a preliminary comparison of these alloys under such ideal conditions.

### 3.1. Receiver characteristics

The external tubular receiver of a SPT plant is studied. It is placed at the top of a 130 m tower and presents an 8.4 m diameter cylindrical structure that frames the panels containing the vertically disposed tubes. In this case, the number of panels,  $N_p$ , is fixed in 18 and the external tube radius,  $b$ , is set in 1.12 cm. The adjacent tubes of a panel are separated 1.9 mm. All of this results in 61 tubes per panel,  $N_t$ . The tubes, seamless, are 1.2 mm thick,  $th$ , and 10 m long,  $L_t$ . The distance selected between the guiding clips, which prevent the tubes from bending excessively, is 2 m, resulting in a total of 6 clips, considering the ones at both ends. The tubes constituting a panel are connected to their respective inlet and outlet headers, which are 1.49 m long, have an external diameter of 0.163 m and a thickness of 2.8 mm. The receiver tubes are painted with a black Pyromark coating in order to increase their absorptivity, which is 0.95 in the visible spectrum [6] and around 0.98 in the infrared spectrum [58]. Its infrared emissivity is temperature dependent, with the data available in Ref. [59]. Opposite to this, the frame cylindrical structure is covered with white Pyromark, a ceramic painting with an infrared emissivity of 0.84 [6] and high reflectivity: 0.8 in the visible spectrum [6] and 0.785 in the infrared one [60]. For the tubes manufacturing, five different alloy alternatives are chosen, in order to compare them: 316H, Haynes 230, Inconel 625, Inconel 740H and Incoloy 800H.

The HTF selected is solar salt (60%  $\text{NaNO}_3$ -40%  $\text{KNO}_3$ ), which is commonly used in most commercial SPT facilities. The solar salt properties as function of the temperature are available in Ref. [6]. There are both a lower temperature limit, 290 °C, and upper one, 565 °C, to prevent its freezing and decomposition, respectively. The HTF is divided into two parallel flow paths, N-S symmetrical, with no crossover between paths. The salt inlet occurs at the bottom of the two northern panels, while the outlet happens at the top of the southern ones. The HTF mass flow through the receiver paths is adjusted to obtain the outlet desired temperature, depending on the heat flux reflected on the receiver surface coming from the heliostat field.

Despite having been omitted in the lifetime analysis, all the piping elements need to be considered in order to properly obtain the pressure drop in the receiver, not just the tubes conforming the panels [35]. Connecting the receiver tubes to their respective inlet and outlet collectors there are three smoothly bended pipes, presenting two 120° elbows and one of 60°, lengths of 0.7, 1.7 and 0.2 m, and a curvature

radius of 0.13 m. Inside these collectors, whose length is 1.4811 m -according to the number of panels of the receiver and diameter of the cylindrical base structure- and its diameter is 162.6 mm, the HTF is modelled to follow a trajectory through two imaginary 90° elbows. Lastly, the connection between adjacent panels occurs through a section with two 90° elbows as well, with lengths of 0.25 m, 0.6 m and 0.17 m diameter, above the 0.1 m minimum recommended [11]. The pressure drop of the receiver would be the maximum between the one obtained for each path, considering the pressure drop through the elements presenting an in-series disposition.

### 3.2. Alloys characteristics

#### 3.2.1. General Overview

The thermal and mechanical properties of the selected materials are obtained from the ASME BPVC Section II Part D [53], with the exception of the yield strength, whose reference is specified for each alloy in the following lines:

- Alloy 316H (UNS 31609) is the high carbon variant of the austenitic stainless-steel grade 316 and is adequate for high temperature applications. At room temperature (RT) it presents a yield strength of 205 MPa [61]. In comparison with other alloys selected, it has poorer mechanical properties and corrosion endurance. Moreover, its use at Solar Two showed issues with stress-corrosion cracking [8]. However, its low price, makes it a potentially interesting alternative. Alloy 316H can only be strengthened by cold work, being thermal treatments discarded for its hardening [62]. This alloy requires annealing at 1040 °C or higher, needing a rapid cooling afterwards.
- Inconel 625 (UNS N06625) is an austenitic nickel-based super-alloy. Although far from other options, it has a better corrosion resistance than 316H. Its yield strength is 502 MPa at RT [63]. It presents great thermal and mechanical properties, which led it to be extensively studied in the industry. Working below 650 °C, it is recommended either hot-finished, cold-finished or annealed [30] while, above such temperature, annealed or solution-treated are preferred, being the latter desirable for demanding applications in terms of rupture or creep. Moreover, alloy 625 has been found to suffer from grain boundary precipitations after being aged at medium temperatures (~650 °C) during low number of cycles (~500h) [63]. This causes it to double its elastic limit and present a perfectly elastic behaviour after the first cycles.
- Inconel 740H (UNS N07740) is an austenitic nickel-base super-alloy extensively used in steam cycles boilers. More recently it has been promoted to sCO<sub>2</sub> cycles, showing an excellent corrosion resistance, balanced with creep strength and weldability [32]. Interest has also arisen in its application in CSP tubular receivers [48]. Its yield strength is the greatest out of the five alloys studied, with 621 MPa at 40 °C [48]. Regarding heat treatments, Inconel 740H is usually provided as solution annealed and age-hardened [64]. The annealing is expected to be performed at 1100 °C for at least 30 min and a maximum of an hour per thickness inch, with water quenching being advisable after it but not mandatory. On the other hand, the aging is done between 760 °C and 815 °C for at least 4 h. The forging or hot-rolling of this alloy are both recommended to be done in a range from 870 °C to 1190 °C. Its price is its main drawback, being the most expensive out of the set studied.
- Incoloy 800H (UNS N08810) is an austenitic nickel-based alloy recommended for corrosive mediums and high temperatures. It was used to manufacture the steam receiver tubes of the Solar One project and also tested by Sandia National Laboratories in a solar salt receiver, prior the Solar Two project [65]. Despite its high corrosion resistance and moderate cost, it has worse mechanical properties than Inconel 625 (230 MPa of yield stress at 40 °C [53]). This alloy is supplied after a high-temperature annealed treatment, which results

in an average grain size of ASTM 5 or coarser and a greater creep and rupture strength than its low-carbon variant [66].

- Haynes 230 (UNS N06230) is an austenitic nickel-base superalloy. Traditionally used in gas turbines, it has recently started being implemented in CSP applications, such as SPT and solar dish, given its great corrosion resistance and since it is thermally more stable compared to alternatives such as Inconel 625 and Incoloy 800H. Nevertheless, it is one of the most expensive alternatives. Its yield stress is 310 MPa at RT [53]. The solution heat-treated for wrought Haynes 230 is done in the temperature range from 1177 °C to 1246 °C, being cooled or water-quenched afterwards. However, annealing in temperatures lower than these range can negatively impact its strength and ductility due to carbide precipitation [31].

The selected alloys are used in this work in the form of seamless tubes, which is typically a more expensive option than the welded alternative but more adequate for applications experiencing high temperature creep, such as the SPT receivers. In the manufacturing process of seamless tubes [67], after the primary melt and remelt, the alloy is forged to the tubular round shape form and extruded. Then, the tubes are cold worked, annealed and aged. Finally, they are straightened and tested. The chemical compositions of these alloys are included in Table 1. Some elements present an admissible range of values within the corresponding alloy composition, others appear in a minimum quantity or are capped at a maximum value. This leaves a certain element, which varies from alloy to alloy, as the one filling the composition up to the 100%, marked in Table 1 as “Balance”.

It is worth noting that the most restrictive temperature in the design phase of the receiver is the film temperature [35]. The limiting value not to be surpassed depends on the HTF selected, aiming to avoid its decomposition, and also depends greatly on the tube material, since it suffers from corrosion. The maximum film temperature allowable for each alloy studied working with molten salt as HTF, according to literature, can be found in Table 2. The 740H alloy, the most recent one out of the five alloys analyzed, presents excellent corrosion properties at high temperatures while in contact with combustion gas and coal ashes,

**Table 1**  
Chemical composition (weight %) of the alloys selected.

Element	230 [31]	316H [68]	625 [30]	740H [64]	800H [66]
Ni	57 Balance	10–14	58 min	Balance	30–35
Cr	22	16–18	20–23	24.5	19–23
W	14	–	–	–	–
Mo	2	2–3	8–10	0.1	–
Fe	3 max	Balance	5 max	3 max	39.5
Co	5 max	–	1 max	20	–
Mn	0.5	2 max	0.5 max	1 max	–
Si	0.4	0.75 max	0.5 max	0.15	–
Nb	0.5 max	–	3.15–4.15 (plus Ta)	1.5	–
Al	0.3	–	0.4 max	1.35	0.15–0.6
Ti	0.1 max	–	0.4 max	1.35	0.15–0.6
C	0.1	0.04–0.1	0.1 max	0.03	0.05–0.1
La	0.02	–	–	–	–
B	0.015	–	–	0.006 max	–
P	–	0.045 max	0.015 max	0.03 max	–
S	–	0.03 max	0.015 max	0.03 max	–
Cu	–	–	–	0.5 max	–

**Table 2**  
Maximum allowable film temperature for the alloys studied.

Alloy	Haynes 230	316H	Inconel 625	740H	800H
$T_{film}$ (°C)	650 [73]	600 [74]	630 [74]	650	650 [75]

**Table 3**  
Alloys prices.

Alloy	230	316H	625	740H	800H
Price (\$/kg)	88	5	70	95	23

which has led it to be widely tested and characterized in the supercritical steam field [69–71]. More recently, interest has been rising involving its application in sCO<sub>2</sub> cycles [32,67], but little to none tests have been carried out when working with molten salt as HTF. However, the presence of a high Cr percentage on its composition, as well as Ni, Co, Ti and Al, which are known to enhance the corrosion resistance, seems to confirm its adequate behaviour at high temperatures in an oxidation environment due to the molten salt use [32,72]. Thus, looking at the rest of alloys studied in this work, their composition and the resulting corrosion resistance, the maximum allowable film temperature for the 740H has been set in 650 °C.

Lastly, the costs per kilogram of each material are comprised in Table 3. The cost of alloy 316H, Inconel 625 and Incoloy 800H tubes, in \$/kg, is supplied by Mtsco [76] for a wholesale purchase. Moreover, the price of alloy 617 is also provided by Mtsco, which is considered to be equivalent to the 740H cost [77]. On the other hand, the price of Haynes 230 has been obtained via energy consulting.

3.2.2. Mechanical coefficients

The coefficients needed in the equations of Section 2.3 have been obtained for the various alloys of this work by adjusting them to the experimental data available in the literature. They are comprised in the tables that follow, which include the references of the experimental data used.

First, Table 4 presents the parameters of the stress-strain curves. The monotonic curve, involving the first load cycle, is fitted to the corresponding Ramberg-Osgood expression [49]

$$\epsilon = \epsilon^E + \epsilon^P = \frac{\sigma}{E} + \left(\frac{\sigma}{K}\right)^{1/n}, \tag{19}$$

while the cyclic curve, related to the stabilized hysteresis loop, is fitted to the Ramberg-Osgood form for said cyclic curve [49,78],

$$\frac{\Delta\epsilon}{2} = \frac{\Delta\epsilon^E}{2} + \frac{\Delta\epsilon^P}{2} = \frac{\Delta\sigma}{2E} + \left(\frac{\Delta\sigma}{2K'}\right)^{1/n'}. \tag{20}$$

The parameters *K* and *n* obtained by fitting Eq. (19) to the monotonic stress-strain experimental data are used in Eq. (7) to calculate the elastic-plastic equivalent stress. On the other hand, the coefficients *K'* and *n'* resulting from the fitting of Eq. (20) to the cyclic stress-strain data are needed in Eqs. (9), (13) and (14). The cyclic parameters for Inconel

**Table 4**  
Coefficients of the stress-strain monotonic and cyclic curves for the elastic-plastic stresses and strains calculation.

Alloy	T (°C)	K (MPa)	n (–)	K' (MPa)	n' (–)	H (MPa)
230 [79]	427	425.75	0.0642	1,455	0.1485	–
	650	303.74	0.0311	760	0.0744	–
316H [80]	427	159.5	0.03	1,246.5	0.239	–
	538	138.9	0.029	1,849.2	0.269	–
	593	181.1	0.066	777.7	0.15	–
625 [63]	650	–	–	–	–	2,332
	750	–	–	–	–	1,287.7
740H [48]	650	975	0.0786	–	–	–
	700	899	0.0584	–	–	–
	750	898	0.0635	–	–	–
800H [21]	427	326	0.1316	–	–	–
	538 [81]	–	–	392	0.0559	–
	649	289	0.1305	–	–	–
	760	182	0.1095	–	–	–
	850 [82]	–	–	178	0.058	–

**Table 5**  
Coefficients of the Norton-Bailey model for the stress relaxation estimation.

Alloy	A (Pa <sup>n<sub>r</sub></sup> s <sup>–1</sup> )	n <sub>r</sub> (–)	m (–)	Q (kJ mol <sup>–1</sup> )	t <sub>stab</sub> (h)
230 [83]	2.688e-45	6.6	0	322 [54]	30
316H [54]	2.0644e-68	11.2594	0	537.64	30
625 [30]	6.78e-95	13.37	0	447	30
740H [84]	5.857e-57	9.6955	0	612.77	30
800H [66]	2.615e-46	9.5	0	685.2	30

740H have not been obtained since its regular operating conditions in a SPT receiver are far from reaching the twice yield strength limit.

For materials showing a bilinear stress-strain interaction, the elasto-plastic modulus, *H*, needed in Eq. (8) to characterize its behaviour is obtained by fitting the stress-strain data above *S<sub>y</sub>* to the expression [50]

$$\epsilon = \frac{S_y}{E} + \frac{\sigma - S_y}{H}, \quad \sigma > S_y. \tag{21}$$

Regarding the alloys selected in this work, Inconel 625 is the one satisfying such scenario [63] and thus the one needing the fit corresponding to Eq. (21).

Table 5 compiles the coefficients obtained for the Norton-Bailey creep strain model, which are needed in Eq. (10) to calculate the stress relaxation. The *m* factor is set to zero, which translates in a simple Norton equation, allowing us to consider secondary creep strain rates. The minimum strain rate (s<sup>–1</sup>) versus stress (MPa) at a fixed temperature plot is used to fit the stress power-law for the creep strain model coefficient (*n<sub>r</sub>*), with the power-law creep equation being:  $\dot{\epsilon} = A_0\sigma^{n_r}$ . The experimental data selected from the literature for this matter have been chosen for the minimum fixed temperature found for every alloy, trying for it to be on par with the working temperatures of the receiver. This has resulted in minimum strain rate versus stress data at fixed temperatures of 600 °C for alloy 316H, 625 °C for Inconel 625 and Incoloy 800H and 700 °C for Haynes 230 and Inconel 740H. Then, the plot of the natural logarithm of the minimum creep rate versus the inverted absolute temperature (K<sup>–1</sup>) at a fixed stress is fitted with the Arrhenius law,  $\dot{\epsilon} = A\sigma^{n_r}\exp(-Q/(RT))$ , to give out the creep activation energy (*Q*) and the constant *A*. Again, the fixed stress selected for each alloy out of the ones available in the literature try to resemble the stress working conditions of each alloy. On the other hand, the stabilization of the stress relaxation in molten salts receiver, *t<sub>stab</sub>*, is typically around 20–30 days [23] which, considering just the most significant hour per day, translates in 20–30 h. In this work, *t<sub>stab</sub>* has been set in 30 h. However, if stress reset occurs, the stabilization time would be considered to be equal to 1 h for the methodology presented in this work. This is so because only the effects of the maximum daily stress relaxation are considered (which lasts 1 h) and the daily shutdown of the installation under these stress reset conditions implies the annulment of the relaxation achieved during the day for the next start-up.

Then, Table 6 comprises the parameters required in Eq. (11) to obtain the rupture time with the M-R-M parametrization. The fit is done with the data available in the rupture time versus stress plots for the different test temperatures.

**Table 6**  
Coefficients of the Mendelson-Roberts-Manson parametrization for the rupture time calculation.

Alloy	β <sub>0</sub>	β <sub>1</sub>	β <sub>2</sub>	β <sub>3</sub>
230 [85]	–26.27	44,158	4.72	–11,337
316H [21]	–35.27	47,957	9.94	–15,175
625 [30]	–44.2641	65,825	12.2	–20,289
740H [64]	–67.74	87,260	20.12	–26,560
800H [66]	–19.78	36,566	–0.9252	–6,197

**Table 7**  
Fatigue coefficients.

Alloy	T (°C)	$\sigma_f'/E$ (%)	$\varepsilon_f'$ (%)	$c_1$ (-)	$c_2$ (-)
230 [86]	427	0.2	18	0.01	0.45
	538	0.2	45	0.0005	0.6
	649	0.2	45	0.001	0.65
316H [21]	427	0.13	5.6	0.023	0.43
	482	0.1	4.95	0.015	0.46
	593	0.078	4.73	0.009	0.5
	705	0.067	3.17	0.01	0.48
625 [87]	650	0.21	4.56	0.014	0.34
	815	0.15	4.92	0.01	0.39
740H [88]	700	0.3	4.11	0.018	0.34
800H [66]	540	0.17	37.6	0.025	0.55
	650	0.2	54	0.003	0.68
	760	0.11	32.4	0.14	0.6

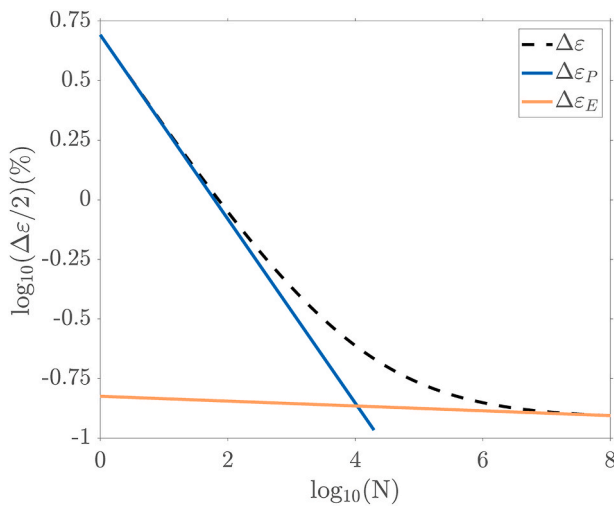


**Fig. 2.** Logarithmic half strain range versus number of allowable cycles plot for Inconel 625 at 815 °C, showing the plastic and elastic regions, useful for the fatigue behaviour characterization of the material.

Lastly, the fatigue parameters to obtain the number of allowable cycles via Eq. (16) are included in Table 7. The fitting is done using the experimental half strain range (%) versus cycles to failure charts found in the literature. With the  $\log_{10}$  plot, see Fig. 2, the tangent line to the curve at low number of cycles allows the calculation of  $c_2$  and  $\varepsilon_f'$  as its slope and the tenth power of its independent coordinate, respectively. On the other hand, the tangent line at high number of cycles does the same for  $c_1$  and  $\sigma_f'/E$ .

### 3.3. Design day and field aiming

The heliostat field is constituted by 2,650 heliostats of 115.8 m<sup>2</sup>, giving a total mirror area of 306,605 m<sup>2</sup>; the field location selected in FluxSPT is the one corresponding to Gemasolar (Seville, Spain). Thus, the day selected to perform the analysis corresponds to the spring equinox in the northern hemisphere. It is a clear day, free of cloud passages and other transient interruptions. It consists of eleven sunlight hours, from 7:00h to 17:00h. Its interaction with the heliostat field results in an hourly symmetrical heat flux distribution on the receiver between the two paths: the 7:00h for the East receiver path is the same than the 17:00h for the West one, the 8:00h for the East path corresponds to the 16:00h for the West half, and so on, being the 12:00h symmetrical in the N-S direction. The hourly DNI of this design day presents a maximum value of 931.6 Wm<sup>-2</sup> at 12:00h and a minimum of

559.2 Wm<sup>-2</sup> at 7:00h and 17:00h. Hence, given the receiver location and orientation, the heat flux on its surface during the morning hours is mainly concentrated on the western half and in the afternoon, it is mostly incident on the eastern one. While the single design day approach considering the spring equinox has been found to underestimate the receiver lifetime with respect a set of days in around 8% in the northern panels [89], as well as considering an hourly analysis instead of more precise time resolutions, it is a reasonable methodology to compare the described alloys under the same operation conditions without heavily increasing the computational cost.

Moreover, the aiming of the heliostat field on the receiver surface can go from an equatorial one to a flat one. To select the appropriate aiming strategy for each receiver configuration it must be considered that there are certain limitations that set the allowable flux density (AFD) on the receiver. These parameters that need to be watched prior the lifetime analysis are: the film temperature, the salt velocity and the pressure drop from the thermal and hydrodynamic analysis, and the twice yield stress from the stress analysis. As for surpassing the twice yield strength limit, this would mean that the alloys in that situation would work in reverse plasticity regime, leading them to be subjected to dynamic aging and material hardening, increasing the stress amplitude with the number of cycles. Opposite to the elastic shakedown, occurring between  $S_y$  and  $2S_y$ , which causes plastic deformation only in the first one or in a few cycles before the elastic stabilization, the reverse plasticity regime does cause plastic yielding in each cycle, which is ill-advised for the receiver to last as much as expected. Hence, as starting point, the aiming strategy chosen in all the cases is  $k = 3$ , with the goal of obtaining the maximum thermal power out of the receiver. However, being the most aggressive one and considering the temperature and stresses limitations to guarantee the safe plant operation, it might not be suitable for all the alloys and all the hours. Consequently, the  $k$  factor would need to be reduced in the cases where the maximum film temperature or the twice yield strength limit are exceeded.

## 4. Results and discussion

The results from the integral analysis of the receiver are exposed and discussed in the present section. The starting point is to set the maximum aiming factor allowable at each hour for every alloy by performing both the thermal analysis and the elastic stresses one, considering the aforementioned limitations in such regard. Upon having established such hourly aiming strategy, the lifetime analysis is performed in terms of the creep and fatigue damages, which require the obtaining of the elastic-plastic stresses and strains. In the former case, the stress relaxation effects have been included. Lastly, a cost analysis of the receiver is undertaken by establishing a set of expected lifecycles for its operation. The panels substitutions that may be required to fulfil these operation periods, as well as the costs associated with these replacements, are considered in this preliminary study under ideal day conditions.

**Table 8**

Hourly maximum aiming strategy factor and heliostat field maximum availability considering the maximum admissible film temperature and twice yield strength limits.

Time	Haynes 230	316H	Inconel 625	740H	800H
7:00	3	1.8 (72%)	2.5	3	3
8:00	2.3	2.0 (43%)	1.5	2.3	2.3
9:00	2.1	2.2 (35%)	2.2 (73%)	2.0	2.1
10:00	2.1	2.3 (35%)	2.3 (69%)	2.0	2.1
11:00	2	2.3 (34%)	2.3 (73%)	2.2	2.3
12:00	2	2.3 (35%)	2.3 (76%)	2.4	2.4
13:00	2	2.3 (34%)	2.3 (73%)	2.2	2.3
14:00	2.1	2.3 (35%)	2.3 (69%)	2.0	2.1
15:00	2.1	2.2 (35%)	2.2 (73%)	2.0	2.1
16:00	2.3	2.0 (43%)	1.5	2.3	2.3
17:00	3	1.8 (72%)	2.5	3	3

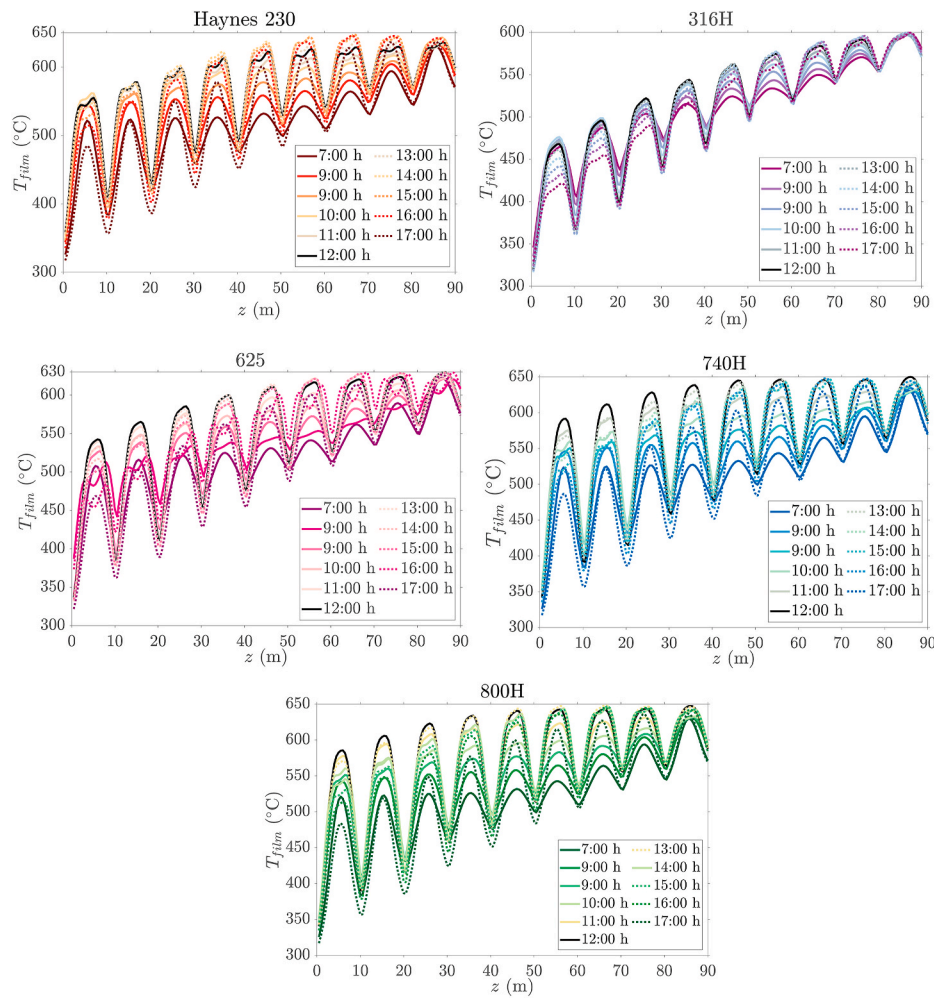


Fig. 3. Maximum film temperature for every alloy, depicted hourly.

#### 4.1. Maximum aiming factor allowable (allowable solar flux)

First, the receivers studied are characterized using the heliostat field and thermal models presented in Section 2.1. The maximum film temperature obtained from such analysis must be kept under the safety limit specified for each alloy, which can be controlled decreasing the aiming factor of the heliostat field. With the availability of the whole field it was found that two of the five alloys selected were not able to meet the limitation criterion imposed by such maximum film temperature allowable, regardless the aiming factor chosen. Evidently, they are the ones with the most restrictive limitation: 316H and Inconel 625. To be able to properly function with these two receivers, the heliostat field availability was reduced (this means that only a percentage of the heliostat field is aiming to the receiver surface) until the limiting film temperature was not surpassed in any case. The maximum availabilities using the flattest aiming strategy, which changes hourly, in these critical cases and hours are also included in between parenthesis and in italics in Table 8. For the scenarios that present no issues, the field availability is not indicated since it is 100%.

After the thermal analysis is performed, the elastic stresses and strains on the receiver can be obtained following the method presented in Section 2.2, using the aiming factors that successfully meet the  $T_{film}$  limit, to check the  $2S_y$  restraint. These elastic stresses are caused by the circumferential, radial and axial thermal gradients on the tube wall, the mechanical restrictions that, despite allowing its axial displacement, prevent the tubes excessive bending and the pressure stresses caused by the HTF inside of them. The higher elastic stresses are present in the

alloys with the highest  $T_{film}$  limit value, which are Haynes 230, Inconel 740H and Incoloy 800H, since it allows more demanding aimings. They are followed by Inconel 625 and in the last place by alloy 316H, with the least permissive  $T_{film}$  limit. It was observed that, for the alloys Haynes 230, 316H and Incoloy 800H, the twice yield strength value was surpassed, which means that they worked in reverse plasticity regime. In the case of Haynes 230, this occurs just at 11:00h, 12:00h and 13:00h with the aimings set from the thermal analysis, and just for the first two panels. Thus, it is not extremely critical and it can be successfully reversed by decreasing the aiming strategy factor obtained from the thermal analysis at these specific hours. However, for Incoloy 800H the issue with twice the yield strength is more severe due to its low  $S_y$ . In addition, for this alloy, it happens for nearly all the panels and from 7:00h to 17:00h, not being feasible to lower that much the equivalent elastic stress by modifying the aiming strategy and the field availability. For alloy 316H, the elastic stress is not as high as the one obtained for Incoloy 800H, being closer to its  $2S_y$ , but the heliostat field availability was already working quite below its full capacity due to the  $T_{film}$  limitation and thus this scenario cannot be avoided for this material neither. Consequently, the final aiming factors leading to the operation under, resulting from considering the  $T_{film}$  and the  $2S_y$  restrictions are included in Table 8.

Now, the resulting evolution of the maximum film temperature, obtained for the final hourly aiming strategies, is presented in Fig. 3 following the eastern HTF path. Thus, the first panel is comprehended between  $z = 0$  m and  $z = 10$  m, panel two between  $z = 10$  m and  $z = 20$  m, and so on. The behaviour of the western panel, given the hourly

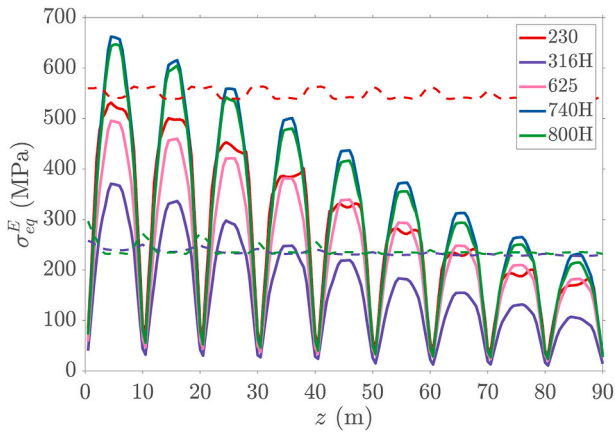


Fig. 4. Equivalent elastic stress at the tube crown at 12:00h for the different alloys under the aiming strategies of Table 8. The 2Sy limit of alloys Haynes 230, 316H and 800H is included in dashed lines.

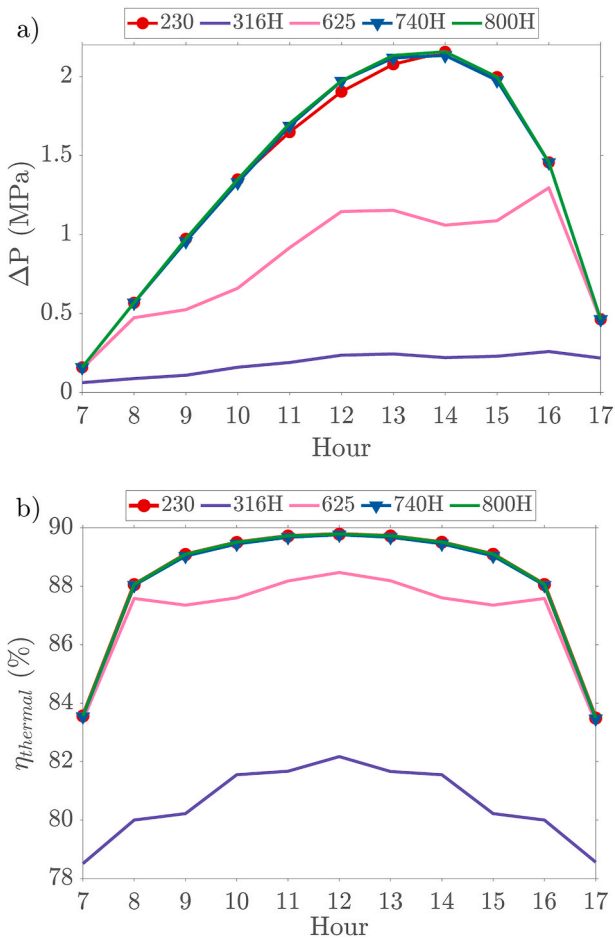


Fig. 5. Hourly depiction of a) Pressure drop in the eastern path and b) Receiver thermal efficiency.

symmetry of the design day with respect to the N-S direction, is the same than the eastern one but inverted with respect to time. As mentioned earlier, it can be sensed through this Figure the greater amount of concentrated heat flux on the eastern half at the afternoon over the morning, given the greater the temperatures on the tube during these hours. Note that the  $T_{film}$  for the central hours of the day for Haynes 230 receiver is slightly below its limit since an aiming factor reduction was

Table 9

Receiver thermal power yielded by each receiver during the design day.

Alloy	Haynes 230	316H	Inconel 625	740H	800H
Thermal Power (MWt)	115.97	40.82	89.72	116.18	116.64

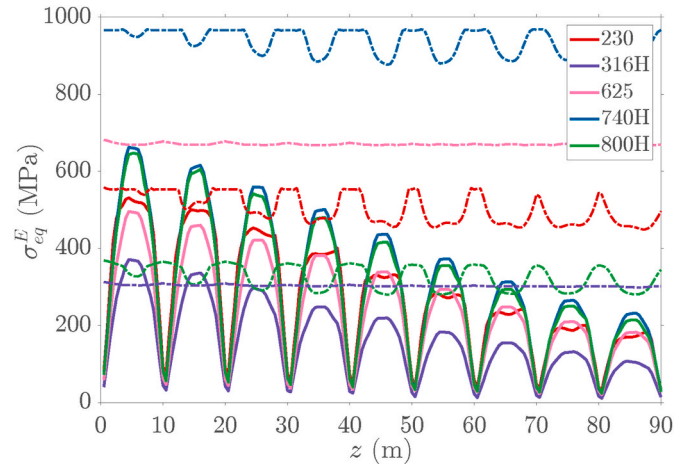


Fig. 6. Equivalent elastic stress at the tube crown at 12:00h and the corresponding stress reset limit for each alloy.

required after the stress analysis to meet the 2Sy limit criterion.

Then, the elastic stresses at the tube crown, which is the most critical spot [36], for the alloys selected at their corresponding aiming strategy and heliostat availability are presented in Fig. 4, following again the eastern HTF path. The hour selected has been the 12:00h since it is one of the most aggressive, jointly with 11:00h (and 13:00h, mirrored), and because of the symmetry between the two flow paths. The twice yield strength value is also included (dashed lines), evaluated at the corresponding temperature for each cell) for the problematic alloys in this regard, showing that Haynes 230 is now below such limit and alloy 316H and Incoloy 800H remain above it.

Once the aiming strategies have been set according to the AFD limits, and before advancing to other stress and lifetime issues, additional receiver critical factors need to be watched, such as the pressure drop on the receiver or the maximum HTF velocity. The higher the pressure drop on the receiver, the higher the pumping power required to operate it, causing the increase of the parasitic losses of the plant. An acceptable value for such maximum pressure drop is around 20 bar [35], with the receiver studied operating around these conditions in the worst scenarios in such regard (Haynes 230, 740H and 800H). Fig. 5 a) depicts the hourly results through the eastern half, with the western one behaving symmetrically. The velocities of the HTF through the receiver present the same hourly evolution as the pressure drop, given their relation; the maximum value is just shy of 6 m/s, also obtained for the alloys with the maximum pressure drop.

Lastly, given that very different aiming strategies and heliostats availabilities must be adopted so the AFD limits are not surpassed, it is useful to provide the thermal efficiency, and thermal power of the set of receivers analyzed. The thermal efficiency in each case is shown in Fig. 5 b), with the thermal power presenting the same trend. To get a better sense of the difference between each receiver configuration in terms of thermal power, the ones obtained during the design day for the different receivers are comprised in Table 9. It is observed that the three alloys with the most similar aiming factors allowable -Haynes 230, 740H and 800H- present both the higher thermal efficiency and thermal power. This can be explained by their higher film temperature limit with respect to the rest of the alloys studied. Consequently, the following receiver in

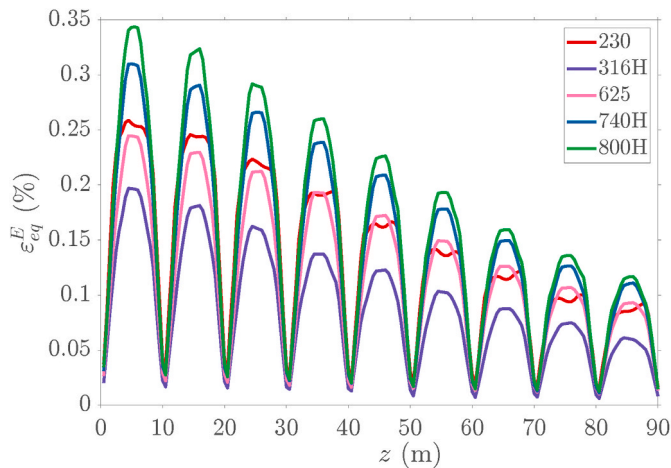


Fig. 7. Equivalent elastic strain at the tube crown for the different alloys at 12:00h.

terms of such power and efficiency is the one in Inconel 625, with a film temperature limit of 630 °C, and the worst one is 316H alloy, highly penalized by its low thermal corrosion limit.

#### 4.2. Creep-fatigue results: lifetime analysis

##### 4.2.1. Equivalent elastic stresses and strains

In the previous section, the equivalent elastic stresses were obtained to set the maximum aiming factor allowable in the receiver surface. Subsequently, it has been checked if the maximum equivalent elastic stress obtained with the hourly aiming configuration of Table 8 is below the shakedown stress range, ( $\Delta\sigma \leq 2S_y$ ).

By contrast, the stress reset limit ( $S_{y,cold} + S_H$ ) has not been considered as a limiting factor in terms of the aiming strategy selection, but it will determine the way the alloys respond in regard to the stress relaxation. With the final aiming strategy, Haynes 230 exhibits no issues in this aspect, as well as alloys Inconel 625 and Inconel 740H (see Fig. 6). On the contrary, both alloys 316H and Incoloy 800H surpass the stress reset limit at certain positions along the flow path and thus these will suffer from stress reset after the daily shutdown of the plant. Even if some  $z$  position does not present elastic stresses above the stress reset limit at certain hours of the day, if such value is exceeded at least once during the daily operation, such receiver spots are still regarded to work under stress reset. For instance, the alloy 316H receiver only shows stress reset at the central sections of the first two panels (panel one from  $z = 0$  m to  $z = 10$  m and panel two from  $z = 10$  m to  $z = 20$  m), while the receiver in 800H presents issues in up to the seventh panel, with at least one spot working under stress reset at a certain time. The rest of the axial positions would relax under the shakedown to elastic cyclic conditions, just as the totality of the Haynes 230, Inconel 625 or Inconel 740H receivers do.

On the other hand, the elastic strains, needed for the fatigue damage calculation, are presented in Fig. 7, again following the HTF path and at 12:00h. The maximum strain is roughly a 0.35% for Incoloy 800H, the alloy presenting the greater ones. This implies that these alloys are way below concerning strain values for fatigue damage.

##### 4.2.2. Equivalent elastic-plastic stresses, stress relaxation and creep stresses

Once the elastic stresses are known, the elastic-plastic stresses are calculated by following the methodology in Section 2.3.1 and using the monotonic and cyclic coefficients, compiled at Table 4, obtained for the different alloys by fitting the manufacturers and experimental data available in the literature. Subsequently, the stress relaxation is obtained with such equivalent elastic-plastic stress, which finally gives out the creep stress.

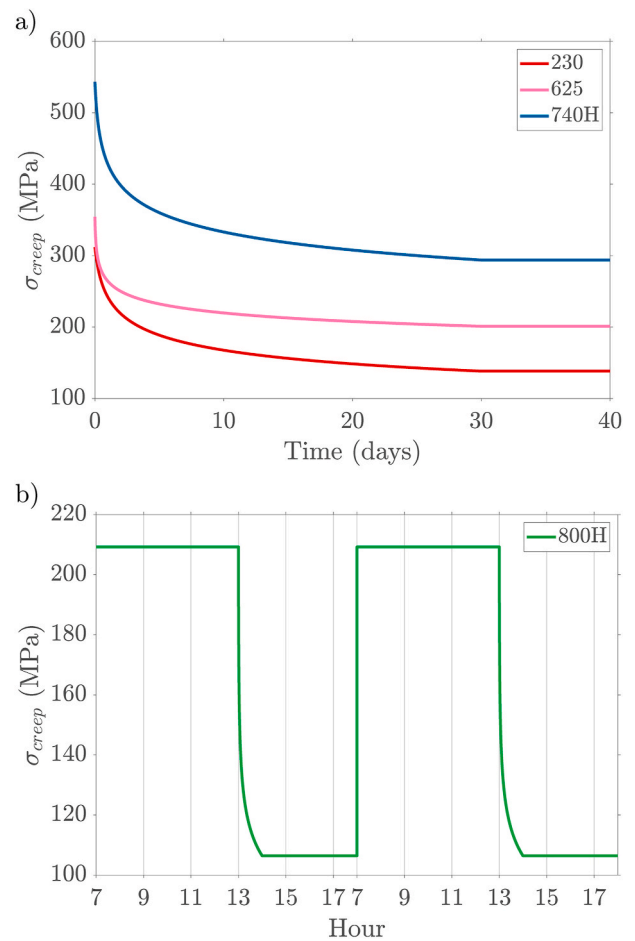


Fig. 8. a) Creep stress achieved after full relaxation for Haynes 230, Inconel 625 and Inconel 740H, working under the shakedown to elastic cyclic regime. b) Creep stress after relaxation for Incoloy 800H, working in stress reset regime, for two consecutive operating days.

As mentioned during the methodology exposition, the stress relaxation at a certain height working below the stress reset limit remains the same during the whole day since it is evaluated at the  $T$  and  $\sigma_{eq}$  combination resulting in the greatest value, out of the ones obtained hourly from the operation of the receiver under the aiming strategies at Table 8. Conversely, for the spots of the receivers in alloy 316H and Incoloy 800H above the stress reset limit, the stabilization time results, from a practical point of view, in 1 h since they suffer from stress reset after the daily shutdown. Hence, in such scenario, instead of considering the stress relaxation effects during the whole day, they are only accounted after the hour at which the maximum relaxation occurs. With that in mind, the final creep stress is obtained by means of Eq. (6). An instance of the stress relaxation behaviour for each alloy is depicted in Fig. 8. Alloy 316H has been omitted since it barely relaxes due to its mild working conditions. On the one hand, Fig. 8 a) shows the stress relaxation influence on the creep stress for Haynes 230, Inconel 625 and Inconel 740H over 40 days. This is enough time to capture the full stress relaxation of these alloys during their cyclic operation, given that their  $t_{stab}$  has been set to 30 h. This is equivalent to 30 days since the relaxation is accumulated just 1 h per day considering a continuous exposure to the maximum temperature [23]. In the three cases, the  $z$  position selected to show its relaxation is the one reaching the greatest value in the whole receiver. For Haynes 230, such location is  $z = 54$  m (sixth panel) and happens at 14:00h. Inconel 625 reaches the maximum relaxation at  $z = 46$  m (fifth panel) and at 13:00h. Lastly, Inconel 740H is illustrated with the 12:00h of  $z = 26$  (third panel). After the  $t_{stab}$ , the

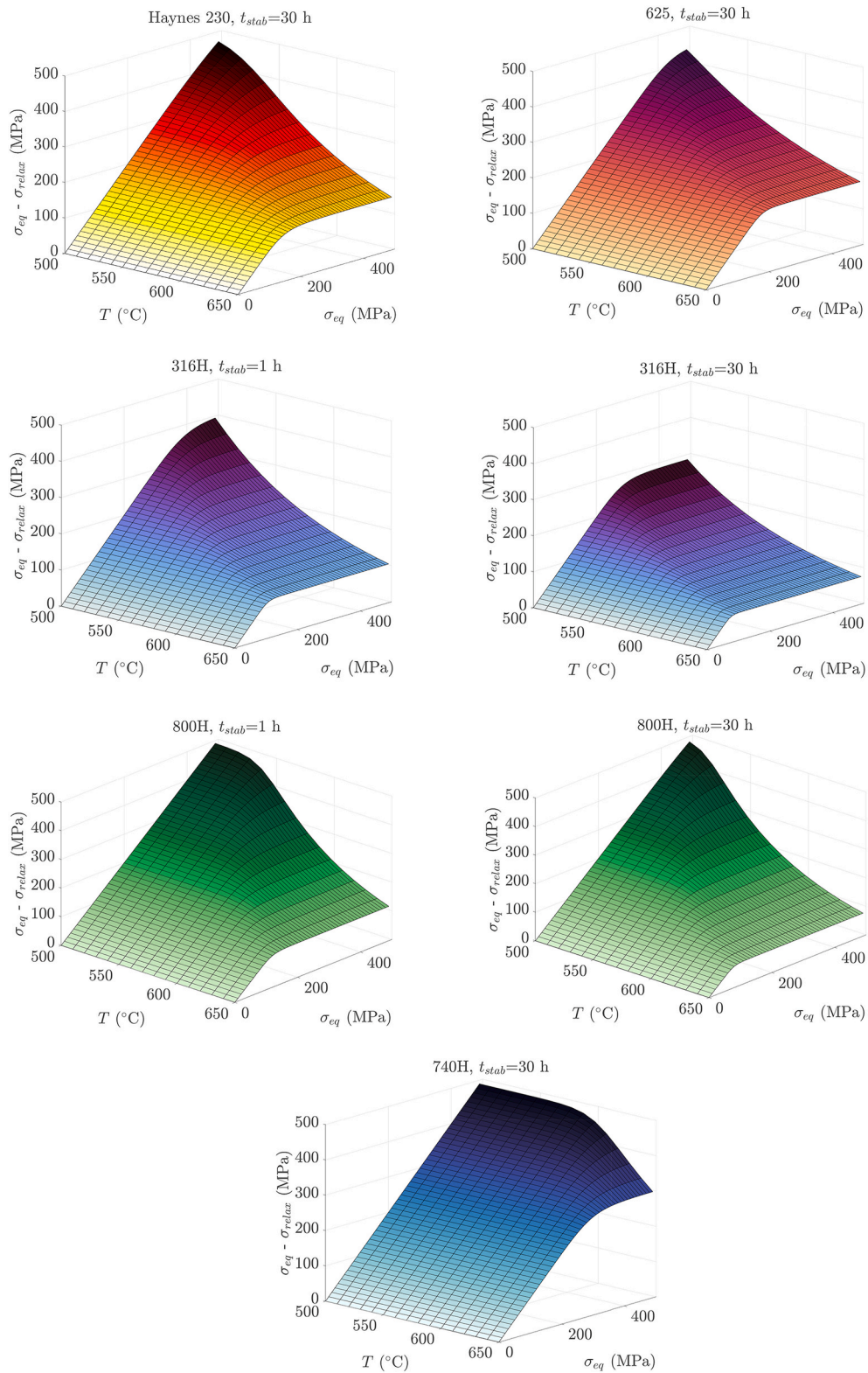


Fig. 9. Effect of stress relaxation in terms of the creep stress as function of the temperature and elastic-plastic equivalent stress solicitation.

stress relaxation is considered fully deployed and hence the following days present a constant value of it; then, that is the stress relaxation that would be finally used in Eq. (6) for the corresponding  $z$  in each case and during all of the daily operation hours. The same procedure is followed for the rest of the axial positions, using their maximum stress relaxation during the day.

On the other hand, Fig. 8 b) depicts an instance of the stress relaxation behaviour under stress reset conditions at the  $z = 46$  m (fifth panel) spot of the Incoloy 800H receiver, which coincides with the maximum relaxation obtained on such receiver and indeed works under stress reset. In this case, the operation hours of two consecutive days have been presented to show the stress reset effect. Hence, looking at

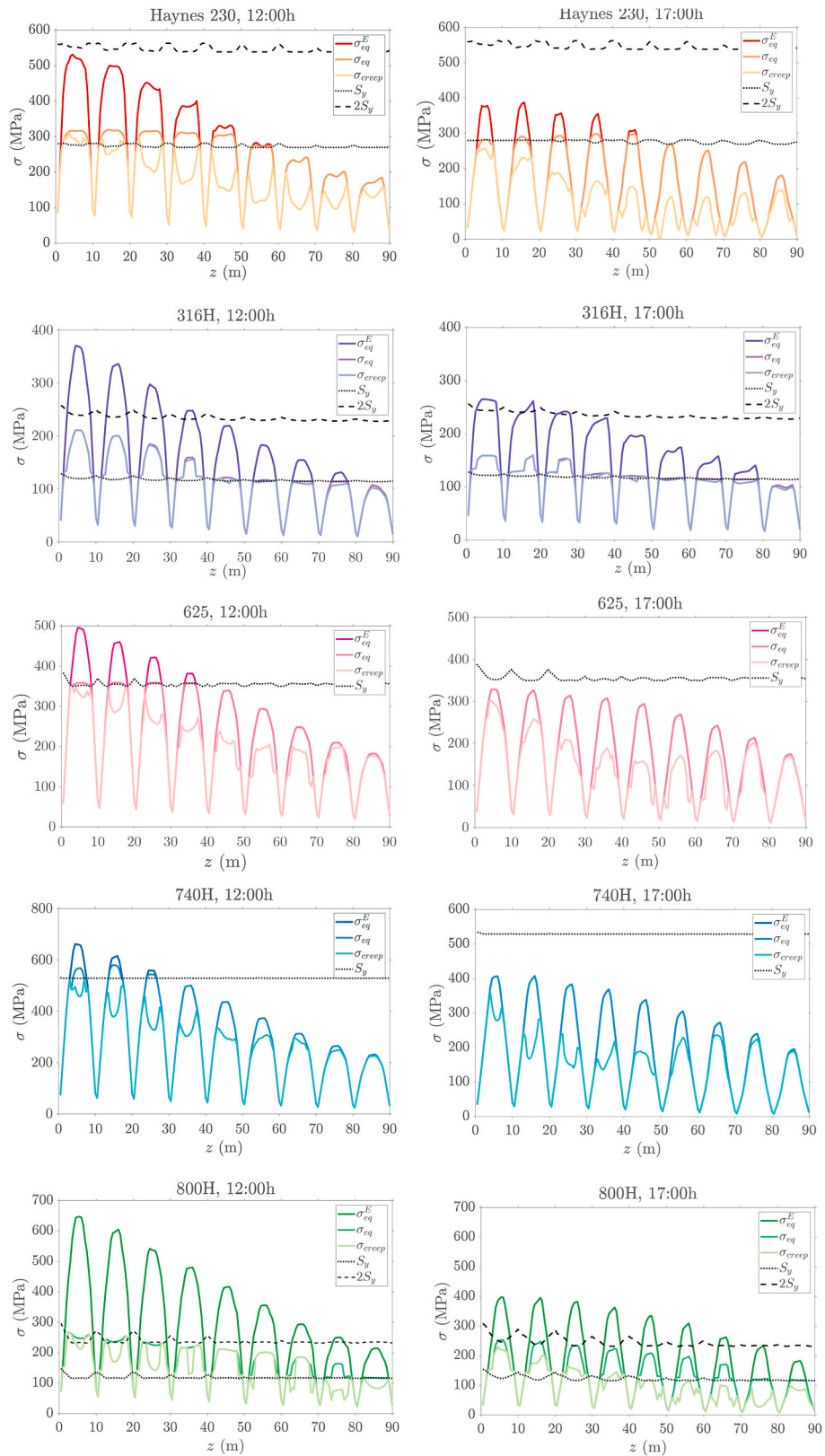


Fig. 10. Elastic stress, elastic-plastic equivalent stress and creep stress for the alloys studied at the tube crown, at 12:00h and at 17:00h.

such Figure, it becomes evident that the criterion to set in the spots surpassing  $S_{SR}$  is to consider the stress relaxation only after the time at which the maximum relaxation occurs (in the  $z$  depicted, from 14:00 to 17:00). The spots that do not fall in the stress reset regime would behave just as the alloys in Fig. 8 a).

Additionally, to get a better sense of the temperature and stress ranges at which every alloy could be able to benefit from the stress relaxation, the creep stress for the studied alloys is depicted in Fig. 9 as a function of the temperature and the equivalent stress solicitation. It has been obtained by using Eqs. (6) and (10) with the coefficients of Table 5

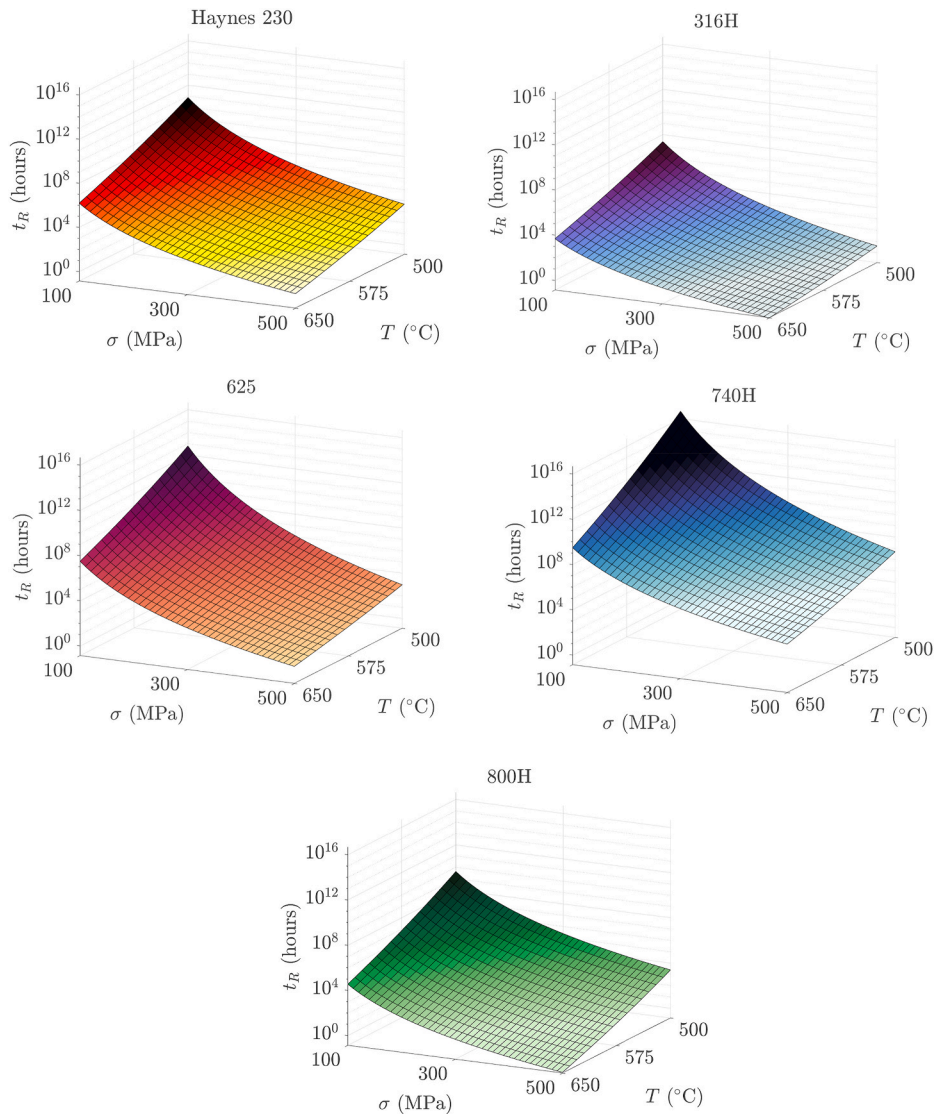


Fig. 11. Rupture time as function of the creep stress and the temperature, which determines the creep damage on the tubes.

at a fixed  $t_{stab}$  of 30 h for all the alloys. It must be noted that when the hold time of the solicitation reaches a high enough value, having a fixed temperature and stress, the stress relaxation becomes constant [51]. Hence, the stabilization time has been selected to fulfill that for all the alloys. In addition, for the two alloys presenting stress reset at certain points, alloy 316H and Incoloy 800H, the creep stress as function of temperature and elastic-plastic equivalent stress has also been depicted for a  $t_{stab}$  of 1 h, capturing how they would behave under such regime. The linear evolution of the resulting  $\sigma_{eq} - \sigma_{relax}$  (or  $\sigma_{creep}$ ), observed in Fig. 9 for certain values of the  $\sigma_{eq}$  solicitation at a fixed temperature, implies that the alloy is not showing stress relaxation at these temperatures and stresses; thus, more aggressive working conditions would be needed for stress relaxation to start happening. It is worth remarking that at a fixed temperature, once the alloy is undergoing through stress relaxation, when increasing  $\sigma_{eq}$  it will continue relaxing in a fashion that implies that  $\sigma_{relax}$  grows proportionally with such solicitation, since the resulting  $\sigma_{creep}$  becomes a constant value. Notable differences can be observed between having a  $t_{stab}$  of 1 h or a  $t_{stab}$  of 30 h, being the latter way more favorable, especially for alloy 316H.

However, it should be noted that the stress relaxation translates in permanent inelastic strains, enlarging the hysteresis loop during hold periods [90] and reducing the alloys fatigue life, although this adverse effect is presumably diminished with the increase of the hold time [91].

Thus, an extremely high stress-relaxation can favor the results of the rupture time in terms of creep, since it reduces the effective creep stress solicitation on the alloy, but it eventually leads to the exhaustion of its ductility [92] and an excess of fatigue, which could cause unexpected early failure not predicted by the creep rupture time. Such conditions are obtained when the stress reset limit is surpassed, where the creep-fatigue damages are combined and the time-to-failure is dramatically reduced.

Lastly, Fig. 10 shows the elastic stress, equivalent elastic-plastic stress and creep stress for the alloys studied at the tube crown at 12:00h as well as 17:00h (eastern path), in order to present a better depiction of the ranges of the different stresses during this particular design day. These 2 h are the ones with the higher and lower  $\sigma_{eq}$ , respectively. This may seem to contradict the fact that the eastern side of the receiver is subjected to a higher concentrated heat flux in the afternoon. However, during the first morning hour, the first panel of this half suffers from a higher peak stress than any panel during the last hour of the afternoon, when the stresses result to be overall higher but more evenly distributed, translating in a slightly lower peak stress despite the greater solar radiation incidence. Alloys Haynes 230, Inconel 625 and Inconel 740H relax normally, under the shakedown to elastic cycling regime, in a greater or lesser deal depending on their characteristics and the temperature and elastic-plastic stress conditions at which they operate. On the other hand, alloy 316H barely relaxes due to its low  $T_{film}$

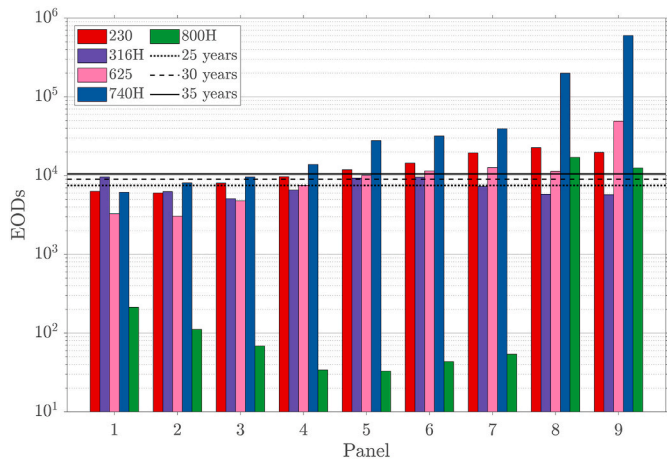


Fig. 12. Equivalent operating days for the alloys studied, working at the spring equinox clear design day conditions, eastern path.

limit, which prevents it from reaching high enough temperatures and elastic-plastic stresses. Moreover, the first two panels, with stress reset, relax roughly 1 MPa. Lastly, note the behaviour of the Incoloy 800H receiver: the creep stress at 12:00h is the same than the elastic-plastic one at middle length of the fifth, sixth and seventh panels; however, they have indeed relaxed at 17:00h. The reason for such outcome is that these spots fall under the stress reset conditions (Fig. 8) and the maximum stress relaxation at these positions occur after midday. This means that since the stress relaxation is only considered for them after the time at which the maximum value occurs and, after the daily shutdown, the following day they will start at their initial stress level, these spots appear not relaxed during the morning hours. Thus, the moment of the maximum stress relaxation is crucial for the alloys with stress reset in this study, since the earlier it happens, the more hours they can benefit from it. In any case such approach errs on the safety side. For the alloys working in the shakedown to elastic cyclic conditions it is irrelevant in such regard since the relaxation is accumulated through the shutdowns and start-ups.

4.2.3. Equivalent operating days

Upon knowing the creep stress, the creep damage can be obtained with the methodology presented in Section 2.3.1. A key aspect of such method is the rupture time calculation, in this case using the M-R-M parametrization with the coefficients in Table 6 for each alloy. In Fig. 11, the rupture time of each alloy is presented likewise it was previously done with the stress relaxation: as a surface depending on the temperature and the stress (Eq. (11)). This representation, made for the same temperature and stress ranges for every case, provides a clearer picture of the creep endurance of each material. As it can be seen in Fig. 11, Inconel 740H presents the greater creep resistance, followed by Inconel 625. The alloys 800H and Haynes 230 present a similar behaviour between them, while alloy 316H has the poorest endurance in this regard. Despite the temperature range on the receiver surface is very limited, with the lower bound of around 500 °C and the upper around 650 °C, and despite these are not especially high temperatures, a great descend on the rupture time is experienced when the temperatures increase from the lower to the upper limit, at a fixed stress. Given the high sensitivity to the temperature and stress that the rupture time has, the regard of the stress relaxation results essential in the lifetime estimation.

With both the creep and fatigue damages, the EODs are obtained for each receiver configurations. Fig. 12 depicts the results for the eastern path. It should be noted that, for the clear design day, the fatigue damage is negligible in comparison to the creep damage, being the latter the limiting factor. A similar outcome has been previously observed in other works available in the literature [23,24,29]. Given the low entropy

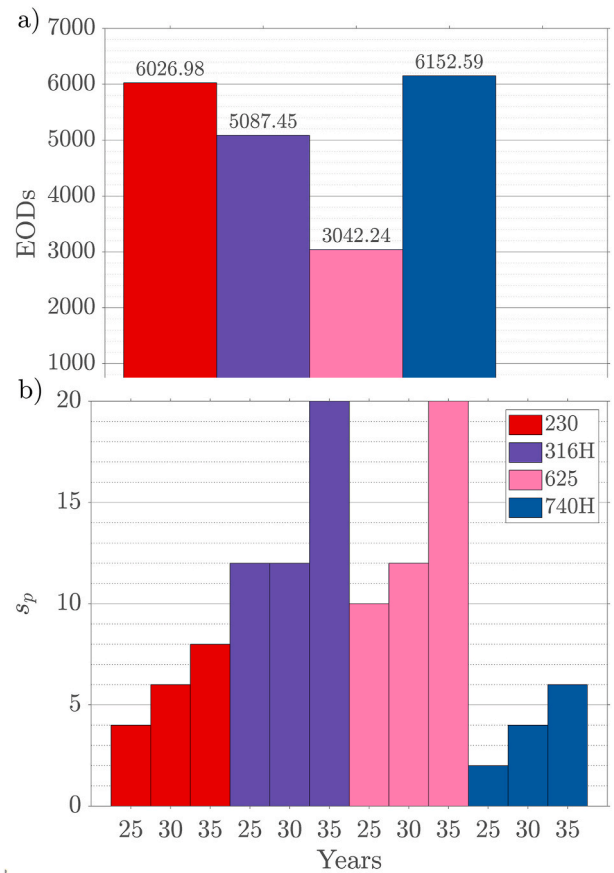


Fig. 13. a) Minimum equivalent operating days for a receiver panel, considering the spring equinox design day. b) Number of total panels substitutions in the different receivers to achieve an operation of 25, 30 and 35 years.

of the fatigue damage in comparison with the creep one, the initial assumption of the  $D_L$  as equal to unity is more than reasonable. In Fig. 12, three reference marks of 25, 30 and 35 years, considering 300 EODs per year, have also been included to analyze the impact of selecting the different alloys in potential plants with different projected lifecycles under the ideal clear design day assumption.

The outcome regarding the EODs obtained highlights the importance of the stress relaxation phenomenon. Looking at the effect that the stress relaxation occasioned in the studied alloys (Fig. 10, difference between  $\sigma_{eq}$  and  $\sigma_{creep}$ ) and given the high sensitivity of the rupture time to the stress applied (Fig. 11), had this effect not been considered, the lifetime of these receivers would have been dramatically reduced, leading to an excessively conservative result. Haynes 230, Inconel 625 and Inconel 740H are the alloys benefitting the most from the stress relaxation since they are working under elastic cyclic shakedown without stress reset. On the other hand, alloy 800H is highly penalized by the stress reset present at the middle length of the first seven panels, with EODs going from 214 days to just 33. Its last two panels, however, benefit from stress relaxation and can last up to 40 years, considering 300 EODs per year. Lastly, alloy 316H is subjected to low elastic-plastic stresses at being insufficient for the material to relax but still low enough to allow an acceptable overall lifetime of the receiver.

The minimum EODs for each receiver are depicted in Fig. 13 a). The limiting panels, understood as the ones presenting the lesser EODs, are the first one for Inconel 740H, the second panel for Haynes 230 and Inconel 625, the third panel in the alloy 316H receiver and the fifth panel in the case of Incoloy 800H. Inconel 740H and Haynes 230 are the two alloys with the higher expected lifetime in their corresponding critical panels, around 20 years. Due to their great corrosion resistance,

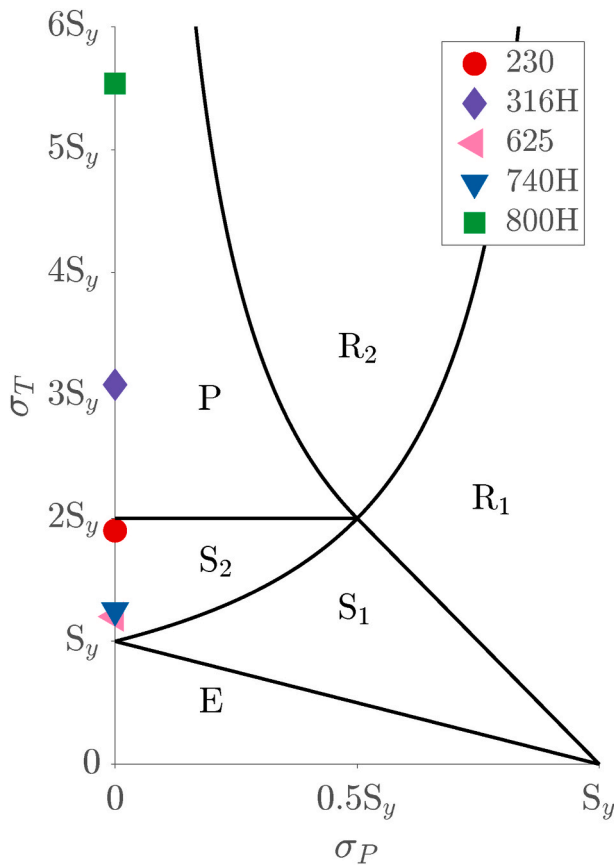


Fig. 14. Stress regimes diagram with the most critical regimes found for each alloy.

these are also two of the three alloys being able to provide with the highest thermal power (Table 9), alongside with 800H, whose poor performance in regard the EODs, the worse out of the five alloys, makes it the least desirable option. Then, alloy 316H is just shy of a 17-year lifetime. Nevertheless, the thermal power it can produce is a 65% less than Haynes 230, 740H and 800H. Lastly, Inconel 625 is the fourth most lasting alloy, with the limiting panel being just over 10 years. Also, it provides around a 24% less thermal power than Haynes, 740H and 800H, but more than twice than alloy 316H.

Subsequently, all the receivers would need panels substitutions to be able to withstand at least a 25-year operation under the present clear design day, which results in a high creep environment for the receiver tubes. The total number of panel substitutions,  $s_p$ , for each receiver are presented in Fig. 13 b) for expected lifetimes of 25, 30 and 35 years. The Inconel 740H receiver would need the substitution of the first panel in both path flows (two in total) to last up to 25 years; from that, the substitution of the second panel of each path and the replacement of third ones would be also required for the receiver to operate 30 and 35 years, respectively. Then, the Haynes 230 receiver needs the substitution of the first two panels of each path (four in total) to operate 25 years; in the same way as the Inconel 740H receiver, the additional replacement of the two third panels and the two fourth panels would be required to reach the 30 and 35-year marks, respectively. Then, alloy 316H demands substitutions for the second, third, fourth, seventh, eighth and ninth panels, making it a total of twelve changes for the whole receiver, to last both 25 and 30 years. When aiming to reach a 35-year lifetime, the first, fifth and sixth panels (and thus, the whole receiver) need replacement as well, plus a second substitution in the third panel. Lastly, despite the limiting panel of Inconel 625 lasting less EODs than 316H, it requires a total of five panel changes per path flow, ten in the whole receiver, when aiming for a 25-year operation: two in the first two

panels and just one on its third panel. However, it should be noted that certain panels require multiple substitutions for this 25-year goal, which alloy 316H does not experiences until the 35-year operation limit. Then, in order to last 30 years, the additional replacement of the two fourth panels is required. For the 35-year mark, the substitution of the fifth panel is needed as well, joined by a third replacement of panels 1 and 2 and a second change of panel 3. Inconel 800H has been excluded from Fig. 13 b) since it would need a total of 830  $s_p$  among the first seven panels of each path just to reach the 25-year mark.

Additionally, it must be noted that exceeding the  $2S_y$  value entails the appearance of large plastic deformations, which can jeopardize the receiver integrity. For such reason, given the alarmingly high elastic stresses at which Inconel 800H and alloy 316H are working, way over  $2S_y$ , their installation is ill-advised. For instance, the first four panels of the receiver in alloy 316H surpass such limit despite presenting acceptable EODs. Moreover, such receiver also needs to operate with unusually low aiming factors and heliostat availabilities in order to fulfill the maximum  $T_{film}$  admissible and so avoid the molten salts corrosive effects on its inner wall, leading it to undesirable low thermal efficiency and power. Looking back, lower carbon variants of these two (and thus, with a poorer creep and rupture properties), Inconel 800 and alloy 316, were the ones used in Solar Two and Solar One respectively, without promising results: Inconel 800 suffered from multiple cracks and alloy 316 was advised to be replaced with an advanced higher nickel alloy.

Related to the regimes at which the alloys operate, Fig. 14 shows where each alloy is located at the Bree diagram [93] in terms of the higher elastic stress that they experience. This diagram depicts the stress regimes that the materials can present as a function of the thermal and pressure stresses with respect to their yield strength  $S_y$ . Given that the pressure stresses (primary stresses) in the receiver tubes are almost negligible with respect to the thermal ones (secondary stresses), none of the cases studied fall inside the ratcheting region, being the elastic (E), the elastic shakedown ( $S_2$ ) and the plastic cyclic regime (P) the only ones relevant in this study.

With all of that in mind, the high lifetime obtained for Inconel 740H makes it the best candidate during the analyzed clear-sky day, which subjects the receiver to aggressive creep conditions. Haynes 230 can match it if the elastic limits are watched. Inconel 625 also presents fairly good results, but its lower corrosion resistance causes it to have a lower thermal efficiency and supply less thermal power than the other two alternatives.

#### 4.3. Receiver costs

To obtain the cost of a SPT receiver expected to last the lifetime periods discussed in the previous section, the prices of the different alloys, included in Table 3, involved in the manufacturing of receiver tubes and headers are multiplied by their weight, the number of them constituting a panel (61 tubes, two headers) and the total panels needed for that specific lifespan, which are the initial amount plus the number of substitutions required during such period, Fig. 13 b).

Also, there are other items whose cost is directly associated with the durability of the receiver tubes, since they need to be replaced with them, such as the coating paint or the different weldings in the tubes. These are relevant in the cost analysis of the receiver from the tubes point of view, especially when dealing with the uneven amount of panel substitutions occurring among the various alloys options. The cost of the Pyromark 2500 ceramic painting is estimated to be around 287 \$/m<sup>2</sup> [58]. Moreover, the cost of its initial application on the receiver tubes and expected reapplications during the receiver lifetime is dissected in Ref. [94], including aspects such as the preparation of the coating and substrate, the application of the coating and other treatments required. These costs (2017) have been adjusted to inflation in this work. On the other hand, the cost of weldings of the tubes to clips and headers, as well as the cost of the nozzles installation in each header are available in

**Table 10**

Receiver costs for lifespans of 25, 30 and 35 years and their resulting cost/power ratio, obtained for the spring equinox design day.

Alloy	Life (yrs)	Thermal power (MWt)	Alloy Price (\$/kg)	Total $N_p$	Total alloy cost (\$)	Total coating cost (\$)	Total specialty cost (\$)	Total receiver cost (\$)	Ratio (\$/MWt)
230	25	115.97	88	22	918,554	580,081	1,349,448	2,848,082	24,559
	30			24	1,002,058	664,755	1,472,125	3,138,939	27,067
	35			26	1,085,563	749,429	1,594,802	3,429,795	29,575
316H	25	40.82	5	30	63,429	684,554	1,840,157	2,588,140	63,404
	30			30	63,429	743,110	1,840,157	2,646,696	64,838
	35			38	80,344	906,139	2,330,865	3,317,348	81,268
625	25	89.72	70	28	883,057	658,436	1,717,479	3,258,973	36,324
	30			30	946,133	743,110	1,840,157	3,529,399	39,338
	35			38	1,198,435	906,139	2,330,865	4,435,439	49,436
740H	25	116.18	95	20	812,523	553,962	1,226,771	2,593,256	22,321
	30			22	893,775	638,637	1,349,448	2,881,860	24,805
	35			24	975,027	723,311	1,472,125	3,170,463	27,289

**Table 11**

Levelized cost of alloy of the receiver alternatives for lifespans of 25, 30 and 35 years considering a clear design day, being Inconel 740H the alloy regarded as the reference one.

Reference	740H				
Alloy	Life (yrs)	$C_{alloy,i}$ (\$/yr)	$E_{alloy,i}$ (MWh/yr)	$C_{ref}$ (\$/yr)	LCOA (\$/MWh)
230	25	36,742	382,701	103,730	0.01
	30	33,402		96,062	0.01
	35	31,016		90,585	0.01
316H	25	2,537	134,706	103,730	0.28
	30	2,114		96,062	0.26
	35	2,296		90,585	0.25
625	25	35,322	296,076	103,730	0.09
	30	31,538		96,062	0.08
	35	34,241		90,585	0.09
740H	25	32,501	383,394	103,730	0
	30	29,793		96,062	0
	35	27,858		90,585	0

Ref. [95], all of them referred to as specialty costs. Each tube is connected to two nozzles and is welded to two headers and six clips. The welding of the tubes-to-header require 1.5 man-hours, the tubes-to-clip ones need 1 h, and the nozzles demand 2 man-hours, with the cost estimated to be of 65 \$/man-hour (2010); this has also been adjusted to inflation, giving a cost of 77.35\$/man-hour. The costs associated with having to shut-down the plant to undertake the panels substitutions are omitted since, with the forecast of their expected lifetime, they can be scheduled in advance to take place in unfavorable operation conditions, such as a series of winter days. If considered, these would penalize the Inconel 625 receiver over the rest of alternatives in the 25, 30 and 35-year lifespans since it presents panels that need to be replaced more than once. Alloy 316 would be penalized only in the 35-year alternative. For the rest of the cases, even if the panels would need to be replaced at different times, a synchronized substitution could be programmed as well.

As a result of all the above, a summary of the different aspects considered in the present costs comparison is shown in Table 10, having omitted the Incoloy 800H receiver due to its poor results, as commented in Section 4.2.3. Moreover, the ratio of the receiver cost over the thermal power that such receiver can produce in the design day is included. Given the disparity found in the operating conditions that these receivers can endure, it is a suitable metric to compare them. The general costs distribution is around a 30% due to the alloy cost, around a 20% due to the coating and a 46–50% due to the specialty costs. The only exception is the alloy 316H receiver, given the extraordinary low price of such material. However, despite that low alloy price, such receiver is highly penalized by the multiple panel substitutions that it must face to fulfill the various expected lifetimes; hence, its total cost ends up being similar to the cost of the receiver in 740H, the most enduring material

but also the most expensive one, and even surpasses it for a 35-year operation. Just one step above these two is the receiver in Haynes 230. The most expensive receiver, the one in Inconel 625, is also handicapped by the various panel substitutions. Moreover, its alloy price is not that far from the most expensive alternatives. Nevertheless, if the thermal power of these receivers is considered, the one in alloy 316H is unarguably the worst performing, followed by the Inconel 625 receiver and the ones in Haynes 230 and Inconel 740H, with the last two being almost on par.

As for the obtention of the LCOA of the studied receivers, the Inconel 740H alternative has been chosen as the reference receiver for being the one providing the lowest cost/power ratio. The LCOA results and the values of the terms involved in Eq. (18) are included in Table 11, with the ones related to the reference receiver appearing in italics. The results show that Haynes 230 LCOA is sustained over the studied lifetime periods. On the contrary, alloy 316H one descends over time, while Inconel 625 presents a minimum in the 30-year mark. Overall, looking at both the LCOA and the cost over thermal power ratio, the extension of the plant operation does not alter the global tendencies in between receivers, being the results very robust in such regard: the best alternative is always the Inconel 740H receiver, followed by the Haynes 230 one, and the worst is the alloy 316H receiver.

## 5. Conclusions

A set of solar power tower (SPT) molten-salt cylindrical central receivers has been analyzed from the lifetime point of view and the costs this implies, them being made of different alloys commonly used in the present or similar applications: 316H, Haynes 230, Inconel 625, 740H and 800H. The analytical model used for that end allows us to estimate the creep-fatigue damage and it is based on experimental data available in the literature. Also, as a part of this work, the corresponding coefficients needed in such model have been obtained for each alloy by fitting the mentioned data.

The analysis is performed for the same clear design day in all the cases, with an hourly time resolution; this constitutes a preliminary analysis, given the ideal nature of the day selected which subjects to the receiver tubes to long periods of time under high creep conditions. Such critical creep is likely to be reduced in real days, with fluctuating direct normal irradiance (DNI) and less hours of operation, which would cause the results to differ under real receiver operation. It should be determined then the extent of these divergences in further analysis, shedding light on whether the obvious quantitative differences with respect the clear day would be joined by qualitative ones, causing a different alloy to be preferred over the others. During the analysis carried out in this work, both the limitation of the film temperature to avoid the salt excessive corrosive effects, and the look for the elastic shakedown regime working conditions (elastic stresses below twice the yield strength,  $2S_y$ ), impose the need of using different aiming strategies, and even heliostat field availability, for each receiver, causing a disparity in

**Table 12**

Summary of the most relevant characteristics and results of the alloys studied during the clear design day.

Alloy	230	316H	625	740H	800H
Corrosion resistance	High (650 °C)	Low (600 °C)	Medium (630 °C)	High (650 °C)	High (650 °C)
Yield strength	Medium	Low	High	High	Low
Thermal power production (MWt)	115.97	40.82	89.72	116.18	116.64
Stress reset	No	Yes	No	No	Yes
Minimum equivalent operating days (EODs)	6,027	5,087	3,042	6,153	33
Total panel substitutions (30 years)	6	12	12	4	–
Levelized cost of alloy (30 years) (\$/MWh)	0.01	0.26	0.08	0	–

the thermal power these receivers can offer. Especially critical is the case of the 316H alloy, whose low maximum admissible film temperature ( $T_{film}$ ) set its thermal power to be around just one third of the maximum one obtained for the set of receivers. For the same reason, the next receiver on the list in terms of thermal power is the Inconel 625, being the Haynes 230, the 740H and the 800H receivers the best alternatives in this regard. Their film temperature and yield strength requirements, as well as the subsequent thermal power production, are compiled in Table 12 for reference.

Upon having established the aiming strategies, the effective creep stresses can be obtained, taking into account the stress relaxation in each case, which enables us to obtain the creep damage on the receiver more accurately. In this case, the receivers in alloys 316H and 800H have the great disadvantage of working under stress reset conditions ( $\sigma_{eq}^E > S_{y,cold} + S_H$ ), as shown in Table 12, not being able to accumulate stress relaxation over consecutive startup/shutdown cycles. On the other hand, the fatigue damage is negligible in all the receivers due to the clear design day with no transient interruptions. Then, the lifetime results show the clear dominance of the 740H receiver over the rest. Its limiting panel lasts just over 20 and a half years and is the receiver requiring the least amount of panel substitutions to fulfill an operating lifetime of 25, 30 and 35 years. The next best performing receiver is the Haynes 230 one, also lasting just shy of 20 years but requiring the substitution of two more panels with respect to the 740H one in each lifecycle mark. Then, alloy 316H receiver is the one needing the greatest number of panel substitutions for the 25-year operation and is at par with the Inconel 625 receiver for the 30 and 35-year ones. The minimum equivalent operating days (EODs) for the former are 5,087 (around 17 years) and requires multiple substitutions of the same panel just once and for the 35-year lifetime scenario. On the other hand, the Inconel 625 receiver limiting panel lasts only 3,042 (just over 10 years), below half the projected plant lifetime in all the cases. Thus, some of its panels require more than one substitution, even for the 25-year operation, with some of them needing a triple replacement to last up to 35 years. Lastly, the Incoloy 800H receiver performs poorly, with the least lasting panel operating during just 33 EODs. The cited minimum lifetime results for each receiver as well as the number of panel substitutions required for the 30-year horizon are also included in Table 12.

A cost analysis is lastly fulfilled, considering just the receiver elements affected by the panel substitutions -receiver tubes, headers, coating, weldings and nozzles- given the great differences observed in this regard among the receivers. This analysis is also motivated by the big gap in terms of thermal power they can supply. Hence, for the studied clear design day and with these aspects in mind, both Inconel 740H and Haynes 230 receivers validate their suitability over the rest, in

terms of total receiver cost over thermal power and of their levelized cost of alloy (LCOA), despite being the two most expensive alloys, as summarized in Table 12 for the 30-year goal. Moreover, the Inconel 625 receiver overtakes the alloy 316H one, with the latter penalized by its low thermal power and despite the former being more expensive and presenting a lower minimum EODs mark.

### CRedit authorship contribution statement

**M. Laporte-Azcué:** Methodology, Software, Validation, Resources, Writing – original draft, Funding acquisition. **P.A. González-Gómez:** Methodology, Software, Validation, Resources, Writing – review & editing, Funding acquisition. **M.R. Rodríguez-Sánchez:** Methodology, Software, Validation, Writing – review & editing, Funding acquisition. **D. Santana:** Conceptualization, Resources, Writing – review & editing, Supervision, Funding acquisition.

### Declaration of competing interest

The authors declare that they have no known competing financial interests or personal relationships that could have appeared to influence the work reported in this paper.

### Acknowledgements

This research is partially funded by the scholarship “Ayudas para la formación del profesorado universitario” [grant number FPU-02361] awarded by the Spanish Ministerio de Educación, Cultura y Deporte (MECD), the Spanish government under the project RTI2018-096664-B-C21 (MICINN/FEDER, UE) and the call “Programa de apoyo a la realización de proyectos interdisciplinarios de I+D para jóvenes investigadores de la Universidad Carlos III de Madrid 2019-2020”, under the projects RETOrenovable-CM-UC3M [grant number 2020/00034/001] and ZEROGASPAIN-CM-UC3M [grant number 2020/00033/001], funded on the frame of the Convenio Plurianual Comunidad de Madrid-Universidad Carlos III de Madrid.

### References

- [1] IRENA, *Global Energy Transformation: A Roadmap to 2050 (2019 Edition)*, Abu Dhabi, 2019.
- [2] A. Zurita, C. Mata-Torres, C. Valenzuela, J.M. Cardemil, R.A. Escobar, Techno-economic analysis of a hybrid CSP+PV plant integrated with TES and BESS in Northern Chile, AIP Conf. Proc. (2018) 180013, <https://doi.org/10.1063/1.5067185>.
- [3] M. Mehos, C. Turchi, J. Vidal, M. Wagner, Z. Ma, C. Ho, W. Kolb, C. Andraka, A. Kruizenga, Concentrating Solar Power Gen3 Demonstration Roadmap, Nrel/TP-5500-67464, 2017, pp. 1–140, <https://doi.org/10.2172/1338899>.
- [4] S.H. Madaeni, R. Sioshansi, P. Denholm, How thermal energy storage enhances the economic viability of concentrating solar power, Proc. IEEE 100 (2012) 335–347, <https://doi.org/10.1109/JPROC.2011.2144950>.
- [5] L.G. Radosevich, A.C. Skinrood, The power production operation of solar one, the 10 MWe solar thermal central receiver pilot plant, J. Sol. Energy Eng. 111 (1989) 144–151, <https://doi.org/10.1115/1.3268300>.
- [6] A.B. Zavoico, Solar power tower - design basis document, Tech. Rep. SAND2001-2100 (2001) 148, <https://doi.org/10.2172/786629>.
- [7] J.E. Pacheco, Final Test and Evaluation Results from the Solar Two Project, Albuquerque, New Mexico, 2002.
- [8] R.Z. Litwin, Receiver System: Lessons Learned from Solar Two - Tech, Rep. SAND2002, Albuquerque, NM, and Livermore, CA (United States), 2002, <https://doi.org/10.2172/800776>.
- [9] M. Romero, R. Buck, J.E. Pacheco, An update on solar central receiver systems, projects, and technologies, J. Sol. Energy Eng. 124 (2002) 98–108, <https://doi.org/10.1115/1.1467921>.
- [10] National Renewable Energy Laboratory (NREL), Concentrating solar power projects: power tower projects. <https://solarpaces.nrel.gov/by-technology/power-tower>. (Accessed 6 July 2020) accessed.
- [11] M. Mehos, H. Price, R. Cable, D. Kearney, B. Kelly, G. Kolb, F. Morse, Concentrating Solar Power Best Practices Study, CO, US, Golden, 2020. %0ANREL, <https://www.nrel.gov/docs/fy20osti/75763.pdf>.
- [12] IRENA, *The Power to Change: Solar and Wind Cost Reduction Potential to 2025, 2016*.
- [13] ASME, *Design Guidelines for the Effects of Creep, Fatigue & Creep-Fatigue Interaction, STP-PT-070.*, 2014.

- [14] British Energy Generation, R5, Issue 3 Assessment Procedure for the High Temperature Response of Structures, 2003.
- [15] ASME, ASME Boiler and Pressure Vessel Code, in: Section III, Division 1, Subsection NH., 2004.
- [16] American Society of Mechanical Engineers, ASME FFS-1, Fitness-For-Service, 2007.
- [17] American Society of Mechanical Engineers, ASME Boiler and Pressure Vessel Code. Code Cases: Nuclear Components Code Case N, vol. 47, 1980.
- [18] Babcock, Wilcox Company, Molten Salt Receiver Subsystem Research Experiment Phase 1 - Final Report, vol. 1, Technical, Barberton, Ohio, 1984.
- [19] J.W. Grossman, W.B. Jones, Evaluation of thermal cycling creep-fatigue damage for a molten salt receiver. <https://www.osti.gov/biblio/7170966-evaluation-thermal-cycling-creep-fatigue-damage-molten-salt-receiver>, 1990.
- [20] B.L. Kistler, Fatigue Analysis of a Solar Central Receiver Design Using Measured Weather Data, SAND86-8017., Albuquerque, New Mexico, 1987. <http://prod.sandia.gov/techlib/access-control.cgi/1986/868017.pdf>.
- [21] I. Berman, A.C. Gangadharan, G.D. Gupta, T. V Narayanan, An Interim Structural Design Standard for Solar Energy Applications. SAND79-8183, New Mexico, Albuquerque, 1979. <https://www.osti.gov/biblio/12260659-final-report-phases-i-interim-structural-design-standard-solar-energy-applications>.
- [22] T.V. Narayanan, M.S.M. Rao, G. Carli, Structural design and life assessment of a molten salt solar receiver, *J. Sol. Energy Eng.* 107 (1985) 258–263, <https://doi.org/10.1115/1.3267688>.
- [23] P.A. González-Gómez, M.R. Rodríguez-Sánchez, M. Laporte-Azcúé, D. Santana, Calculating molten-salt central-receiver lifetime under creep-fatigue damage, *Sol. Energy* 213 (2021) 180–197, <https://doi.org/10.1016/j.solener.2020.11.033>.
- [24] T. Conroy, M.N. Collins, J. Fisher, R. Grimes, Levelized cost of electricity evaluation of liquid sodium receiver designs through a thermal performance, mechanical reliability, and pressure drop analysis, *Sol. Energy* 166 (2018) 472–485, <https://doi.org/10.1016/j.solener.2018.03.003>.
- [25] T. Conroy, M.N. Collins, J. Fisher, R. Grimes, Thermal and mechanical analysis of a sodium-cooled solar receiver operating under a novel heliostat aiming point strategy, *Appl. Energy* 230 (2018) 590–614, <https://doi.org/10.1016/j.apenergy.2018.08.113>.
- [26] D.K. Fork, J. Fitch, S. Ziaei, R.I. Jetter, Life estimation of pressurized-air solar-thermal receiver tubes, *J. Sol. Energy Eng.* 134 (2012), <https://doi.org/10.1115/1.4007686>.
- [27] T.W. Neises, M.J. Wagner, A.K. Gray, Structural design considerations for tubular power tower receivers operating at 650 °C, in: Vol. 1 Comb. Energy Cycles, CHP, CCHP, Smart Grids; Conc. Sol. Power, Sol. Thermochem. Therm. Energy Storage; Geothermal, Ocean. Emerg. Energy Technol. Hydrog. Energy Technol. Low/Zero Emiss. Power Plants an, American Society of Mechanical Engineers, 2014, pp. 1–7, <https://doi.org/10.1115/ES2014-6603>.
- [28] K. Nithyanandam, R. Pitchumani, Thermal and structural investigation of tubular supercritical carbon dioxide power tower receivers, *Sol. Energy* 135 (2016) 374–385, <https://doi.org/10.1016/j.solener.2016.05.039>.
- [29] J. Ortega, S. Khivisara, J. Christian, C. Ho, J. Yellowhair, P. Dutta, Coupled modeling of a directly heated tubular solar receiver for supercritical carbon dioxide Brayton cycle: optical and thermal-fluid evaluation, *Appl. Therm. Eng.* 109 (2016) 970–978, <https://doi.org/10.1016/j.applthermaleng.2016.06.031>.
- [30] Special Metals Corp, INCONEL alloy 625, Spec. Met. Datasheets. 625 (2013) 1–28. <https://www.specialmetals.com/assets/smc/documents/alloys/inconel/inconel-alloy-625.pdf>.
- [31] Haynes International, HAYNES 230 Alloy, 2020.
- [32] J.J. de Barbadillo, INCONEL alloy 740H, in: Mater. Ultra-supercritical Adv. Ultra-supercritical Power Plants, Elsevier, 2017, pp. 469–510, <https://doi.org/10.1016/B978-0-08-100552-1.00014-2>.
- [33] G. Augsburger, D. Favrat, Modelling of the receiver transient flux distribution due to cloud passages on a solar tower thermal power plant, *Sol. Energy* 87 (2013) 42–52, <https://doi.org/10.1016/j.solener.2012.10.010>.
- [34] F.J. Collado, Quick evaluation of the annual heliostat field efficiency, *Sol. Energy* 82 (2008) 379–384, <https://doi.org/10.1016/j.solener.2007.10.007>.
- [35] M.R. Rodríguez-Sánchez, A. Soria-Verdugo, J.A. Almendros-Ibáñez, A. Acosta-Iborra, D. Santana, Thermal design guidelines of solar power towers, *Appl. Therm. Eng.* 63 (2014) 428–438, <https://doi.org/10.1016/j.applthermaleng.2013.11.014>.
- [36] M. Laporte-Azcúé, P.A. González-Gómez, M.R. Rodríguez-Sánchez, D. Santana, Deflection and stresses in solar central receivers, *Sol. Energy* 195 (2020) 355–368, <https://doi.org/10.1016/j.solener.2019.11.066>.
- [37] P.A. González-Gómez, J. Gómez-Hernández, J.V. Briongos, D. Santana, Lifetime analysis of the steam generator of a solar tower plant, *Appl. Therm. Eng.* 159 (2019) 113805, <https://doi.org/10.1016/j.applthermaleng.2019.113805>.
- [38] R.Z. Wang, X.C. Zhang, J.G. Gong, X.M. Zhu, S.T. Tu, C.C. Zhang, Creep-fatigue life prediction and interaction diagram in nickel-based GH4169 superalloy at 650 °C based on cycle-by-cycle concept, *Int. J. Fatig.* 97 (2017) 114–123, <https://doi.org/10.1016/j.ijfatigue.2016.11.021>.
- [39] M.J. Reno, C.W. Hansen, J.S. Stein, Global Horizontal Irradiance Clear Sky Models: Implementation and Analysis, New Mexico, Albuquerque, 2012, <https://doi.org/10.2172/1039404>.
- [40] A. Sánchez-González, D. Santana, Solar flux distribution on central receivers: a projection method from analytic function, *Renew. Energy* 74 (2015) 576–587, <https://doi.org/10.1016/j.renene.2014.08.016>.
- [41] A. Sánchez-González, M.R. Rodríguez-Sánchez, D. Santana, Aiming factor to flatten the flux distribution on cylindrical receivers, *Energy* 153 (2018) 113–125, <https://doi.org/10.1016/j.energy.2018.04.002>.
- [42] M.R. Rodríguez-Sánchez, C. Marugán-Cruz, A. Acosta-Iborra, D. Santana, Comparison of simplified heat transfer models and CFD simulations for molten salt external receiver, *Appl. Therm. Eng.* 73 (2014) 991–1003, <https://doi.org/10.1016/j.applthermaleng.2014.08.072>.
- [43] M. Laporte-Azcúé, P.A. González-Gómez, M.R. Rodríguez-Sánchez, D. Santana, Exergy analysis of solar central receivers, *Sol. Energy* 207 (2020) 957–973, <https://doi.org/10.1016/j.solener.2020.07.033>.
- [44] J.N. Goodier, Thermal stress and deformation, *J. Appl. Mech.* 24 (1957) 467–474.
- [45] S. Timoshenko, J.N. Goodier, Theory of Elasticity (1951) 506.
- [46] X. Chen, M.A. Sokolov, S. Sham, D.L. Erdman, J.T. Busby, K. Mo, J.F. Stubbins, Experimental and modeling results of creep-fatigue life of Inconel 617 and Haynes 230 at 850 °C, *J. Nucl. Mater.* 432 (2013) 94–101, <https://doi.org/10.1016/j.jnucmat.2012.08.040>.
- [47] M.D. McMurtrey, Creep-fatigue Behavior and Damage Accumulation of a Candidate Structural Material for Concentrating Solar Power Solar Thermal Receiver, 2019.
- [48] B. Barua, M.D. McMurtrey, R.E. Rupp, M.C. Messner, Design Guidance for High Temperature Concentrating Solar Power Components, 2020, <https://doi.org/10.2172/1582656>.
- [49] G. Glinka, Calculation of inelastic notch-tip strain-stress histories under cyclic loading, *Eng. Fract. Mech.* 22 (1985) 839–854, [https://doi.org/10.1016/0013-7944\(85\)90112-2](https://doi.org/10.1016/0013-7944(85)90112-2).
- [50] A. Mofkhar, A. Buczynski, G. Glinka, Calculation of elasto-plastic strains and stresses in notches under multiaxial loading, *Int. J. Fract.* 70 (1995) 357–373, <https://doi.org/10.1007/BF00032453>.
- [51] X.L. Yan, X.C. Zhang, S.T. Tu, S.L. Mannan, F.Z. Xuan, Y.C. Lin, Review of creep-fatigue endurance and life prediction of 316 stainless steels, *Int. J. Pres. Ves. Pip.* 126 (2015) 17–28, <https://doi.org/10.1016/j.ijpvp.2014.12.002>.
- [52] C. Becht IV, Elevated temperature shutdown concepts, *J. Press. Vessel Technol. Trans. ASME*. 133 (2011) 1–5, <https://doi.org/10.1115/1.4003456>.
- [53] American Society of Mechanical Engineers, ASME Boiler and Pressure Vessel Code, Section II Part D, 2010.
- [54] D.R. Eno, G.A. Young, T.-L. Sham, A unified view of engineering creep parameters, in: ASME (Ed.), ASME Press. Vessel. Pip. Div. Conf. (PVP2008), Chicago, July 27–31, ASME, Chicago, 2008: pp. 777–792. doi:10.1115/pvp2008-61129.
- [55] J. Mao, D. Tang, S. Bao, L. Luo, Z. Gao, High temperature strength and multiaxial fatigue life assessment of a tubeshheet structure, *Eng. Fail. Anal.* 68 (2016) 10–21, <https://doi.org/10.1016/j.engfailanal.2016.05.030>.
- [56] A. Kalnins, Fatigue analysis in pressure vessel design by local strain approach: methods and software requirements, *J. Press. Vessel Technol. Trans. ASME*. 128 (2006) 2–7, <https://doi.org/10.1115/1.2137770>.
- [57] A. Boubault, C.K. Ho, A. Hall, T.N. Lambert, A. Ambrosini, Levelized cost of energy (LCOE) metric to characterize solar absorber coatings for the CSP industry, *Renew. Energy* 85 (2016) 472–483, <https://doi.org/10.1016/j.renene.2015.06.059>.
- [58] C.K. Ho, J.E. Pacheco, Levelized Cost of Coating (LCOE) for selective absorber materials, *Sol. Energy* 108 (2014) 315–321, <https://doi.org/10.1016/j.solener.2014.05.017>.
- [59] W.R. Wade, W.S. Slem, Measurements of Total Emittance of Several Refractory Oxides, Cermet, and Ceramics for Temperatures from 600 Degrees F to 2,000 Degrees F, (no. TN-D-998), Washington DC, 1962.
- [60] J.F. Scannapieco, Irradiation of Thermal Control Coatings, Final Report. NASA-CR-94684, DOC.-68SD4224, 1968.
- [61] B.C. Du, Y.L. He, Z.J. Zheng, Z.D. Cheng, Analysis of thermal stress and fatigue fracture for the solar tower molten salt receiver, *Appl. Therm. Eng.* 99 (2016) 741–750, <https://doi.org/10.1016/j.applthermaleng.2016.01.101>.
- [62] W. Ren, L. Lin, Consideration of thermal embrittlement in alloy 316H for advanced non-light water reactor applications, in: Proc. ASME PVP2019. Vol. 6B Mater. Fabr., American Society of Mechanical Engineers, 2019, pp. 565–568, <https://doi.org/10.1115/PVP2019-93431>.
- [63] L. Mataveli Suave, J. Cormier, D. Bertheau, P. Villechaise, A. Soula, Z. Hervier, F. Hamon, High temperature low cycle fatigue properties of alloy 625, *Mater. Sci. Eng.* 650 (2016) 161–170, <https://doi.org/10.1016/j.msea.2015.10.023>.
- [64] PCC Energy Group, Inconel® alloy 740H: a superalloy specifically designed for advanced ultra supercritical power generation. [http://www.specialmetals.com/files/PCC\\_EG\\_740H\\_White\\_Paper.pdf](http://www.specialmetals.com/files/PCC_EG_740H_White_Paper.pdf), 2014.
- [65] G.J. Kolb, An Evaluation of Possible Next-Generation High Temperature Molten-Salt Power Towers, SAND2011-9320., Albuquerque, New Mexico, 2011.
- [66] Special Metals Corp, INCOLOY alloy 800H & 800HT. <https://www.specialmetals.com/assets/smc/documents/alloys/incoloy/incoloy-alloys-800h-800ht.pdf>, 2004.
- [67] J.J. De Barbadillo, B.A. Baker, R.D. Golluhue, S.A. McCoy, Properties of inconel alloy 740H for high pressure steam and supercritical CO2 applications, in: ASME Symp. Elev. Temp. Appl. Mater. Foss. Nucl. Petrochemical Ind. ETAM2018, 2018, pp. 1–11, <https://doi.org/10.1115/ETAM2018-6741>.
- [68] Atlas Steels, Grade data sheet 316 (2011) 316L, 316H.
- [69] J. Lu, Y. Li, Z. Yang, J. Huang, M. Zhu, Y. Gu, Fireside corrosion behaviors of inconel 740H superalloy in various SO2 contents, in: Energy Mater., Springer, Cham, Switzerland, 2017, pp. 193–201, [https://doi.org/10.1007/978-3-319-52333-0\\_18](https://doi.org/10.1007/978-3-319-52333-0_18).
- [70] K. Luo, C. Li, F. Xue, Y. Liu, L. Zhang, G. Zhang, Oxidation and hot corrosion behavior of inconel 740H alloy at high temperature, in: Y. Han (Ed.), High Perform. Struct. Mater., Springer Singapore, Singapore, 2018, pp. 557–565, [https://doi.org/10.1007/978-981-13-0104-9\\_59](https://doi.org/10.1007/978-981-13-0104-9_59).
- [71] P.S.M. Jena, R.K. Singh, L. Mahanta, S. Paswan, J.K. Sahu, Low cycle fatigue behaviour of nickel base superalloy IN 740H at 760 °C: influence of fireside corrosion atmosphere, *Int. J. Fatig.* 116 (2018) 623–633, <https://doi.org/10.1016/j.ijfatigue.2018.07.018>.
- [72] P.-J. Cunat, Alloying Elements in Stainless Steel and Other Chromium-Containing Alloys, 2004.

- [73] G. McConohy, A. Kruiženga, Molten nitrate salts at 600 and 680°C: thermophysical property changes and corrosion of high-temperature nickel alloys, *Sol. Energy* 103 (2014) 242–252, <https://doi.org/10.1016/j.solener.2014.01.028>.
- [74] A. Miliozzi, G.M. Giannuzzi, P. Tarquini, A. La Barbera, Fluido termovettore: dati di base della miscela di nitrati di sodio e potassio ENEA/SOL/RD/2001/07, 2001.
- [75] R.W. Bradshaw, S.H. Goods, Corrosion of Alloys and Metals by Molten Nitrates, Albuquerque, NM, and Livermore, CA (United States), 2001.
- [76] Mt Stainless Steel (Mtsco), 2020. [www.mtstainlesssteel.com](http://www.mtstainlesssteel.com).
- [77] K. Nicol, Status of Advanced Ultra-supercritical Pulverised Coal Technology, London, UK, 2013.
- [78] Z. Lopez, A. Fatemi, A method of predicting cyclic stress – strain curve from tensile properties for steels, *Mater. Sci. Eng.* 556 (2012) 540–550, <https://doi.org/10.1016/j.msea.2012.07.024>.
- [79] P.R. Barrett, R. Ahmed, M. Menon, T. Hassan, Isothermal low-cycle fatigue and fatigue-creep of Haynes 230, *Int. J. Solid Struct.* 88–89 (2016) 146–164, <https://doi.org/10.1016/j.ijsolstr.2016.03.011>.
- [80] P.S. Maiya, Cyclic Stress-Strain Curves and Cyclic-Hardening Behavior for Types 304 and 316 Stainless Steel and Incoloy Alloy 800H, ANL-80-100, 1980.
- [81] J.L. Kaee, High-temperature low-cycle fatigue of Alloy 800H, *Int. J. Fatig.* 31 (2009) 332–340, <https://doi.org/10.1016/j.ijfatigue.2008.08.002>.
- [82] K.B.S. Rao, H. Schuster, G.R. Halford, Mechanisms of high-temperature fatigue failure in alloy 800H, *Metall. Mater. Trans.* 27 (1996) 851–861, <https://doi.org/10.1007/BF02649752>.
- [83] C.J. Boehlert, S.C. Longanbach, A comparison of the microstructure and creep behavior of cold rolled HAYNES® 230 alloy™ and HAYNES® 282 alloy™, *Mater. Sci. Eng.* 528 (2011) 4888–4898, <https://doi.org/10.1016/j.msea.2011.03.019>.
- [84] S. Zhang, Y. Takahashi, Creep and creep-fatigue deformation and life assessment of Ni-based alloy 740H and Alloy 617, in: Proc. ASME PVP2018, 2018, <https://doi.org/10.1115/PVP2018-85079>.
- [85] D.R. Eno, G.A. Young, T.-L. Sham, A unified view of engineering creep parameters, in: ASME vol. 6, Mater. Fabr. Parts A B, ASME/EDC, Chicago, 2008, pp. 777–792, <https://doi.org/10.1115/PVP2008-61129>.
- [86] M.G. Fahrman, S.K. Srivastava, Low cycle fatigue behaviour of HAYNES 230 alloy, *Mater. A. T. High. Temp.* 31 (2014) 221–225, <https://doi.org/10.1179/1878641314Y.0000000017>.
- [87] T. Bui-Quoc, R. Gomuc, A. Biron, H. Nguyen, J. Masoune, Elevated temperature fatigue-creep behavior of nickel-base superalloy IN 625, in: H. Solomon, G. Halford, L. Kaisand, B. Leis (Eds.), *Low Cycle Fatigue*, ASTM International, 1988, pp. 470–484, <https://doi.org/10.1520/STP24499S>.
- [88] F. Abe, Research and development of heat-resistant materials for advanced USC power plants with steam temperatures of 700 °C and above, *Engineering 1* (2015) 211–224, <https://doi.org/10.15302/J-ENG-2015031>.
- [89] M. Laporte-Azcué, M.R. Rodríguez-Sánchez, P.A. González-Gómez, D. Santana, Assessment of the time resolution used to estimate the central solar receiver lifetime, *Appl. Energy* 301 (2021) 117451, <https://doi.org/10.1016/J.APENENERGY.2021.117451>.
- [90] C.Y. Jeong, S.W. Nam, J. Ginzler, Activation processes of stress relaxation during hold time in 1Cr – Mo – V steel, *Mater. Sci. Eng.* 264 (1999) 188–193, [https://doi.org/10.1016/S0921-5093\(98\)01086-7](https://doi.org/10.1016/S0921-5093(98)01086-7).
- [91] C.R. Brinkman, J.P. Strizak, M.K. Booker, Time-dependent strain-controlled fatigue behavior of annealed 2 1/4 Cr-1 Mo steel for use in nuclear steam generator design, *J. Nucl. Mater.* 62 (1976) 181–204, [https://doi.org/10.1016/0022-3115\(76\)90015-5](https://doi.org/10.1016/0022-3115(76)90015-5).
- [92] W.M. Payten, K.U. Snowden, D.W. Dean, Effects of prior stress relaxation on the prediction of creep life using time and strain based methods, *J. Pressure Vessel Technol.* 135 (2013) 1–8, <https://doi.org/10.1115/1.4023726>.
- [93] J. Bree, Elastic-plastic behaviour of thin tubes subjected to internal pressure and intermittent high-heat fluxes with application to fast-nuclear-reactor fuel elements, *J. Strain Anal.* 2 (1967) 226–238, <https://doi.org/10.1243/03093247v023226>.
- [94] A. Boubault, C.K. Ho, A. Hall, T.N. Lambert, A. Ambrosini, Durability of solar absorber coatings and their cost-effectiveness, *Sol. Energy Mater. Sol. Cells* 166 (2017) 176–184, <https://doi.org/10.1016/j.solmat.2017.03.010>.
- [95] B. Kelly, M. Izygon, L. Vant-Hull, Advanced Thermal Energy Storage for Central Receivers with Supercritical Coolants, Lakewood, CO, 2010, <https://doi.org/10.2172/981926>.